

Effects of Short-Range Correlations in $(e, e'p)$ reactions and nuclear overlap functions

M. Mazziotta, J. E. Amaro and F. Arias de Saavedra

Departamento de Física Moderna, Universidad de Granada, Granada 18071, Spain

Abstract

A study of the effects of short-range correlations over the $(e, e'p)$ reaction for low missing energy in closed shell nuclei is presented. We use correlated, quasi-hole overlap functions extracted from the asymptotic behavior of the one-body density matrix, containing central correlations of Jastrow type, up to first-order in a cluster expansion, and computed in the very high asymptotic region, up to 100 fm. The method to extract the overlap functions is checked in a simple shell model, where the exact results are known. We find that the single-particle wave functions of the valence shells are shifted to the right due to the short-range repulsion by the nuclear core. The corresponding spectroscopic factors are reduced only a few percent with respect to the shell model. However, the $(e, e'p)$ response functions and cross sections are enhanced in the region of the maximum of the missing momentum distribution due to short-range correlations.

PACS: 25.30.Fj; 21.60.Gx 21.10.Jx 24.10.Eq;

Keywords: electromagnetic nucleon knockout; short-range correlations; overlap functions; final state interactions; spectroscopic factors; structure response functions.

1 Introduction

In the last years, quasi-free $(e, e'p)$ reactions have proved to be an ideal tool to study the spectral function of nuclei [1, 2]. Apart from the ambiguities coming from final-state interactions and off-shell effects in the electromagnetic current, it is possible to extract such valuable information about single-particle properties as momentum distributions and spectroscopic factors of the different nucleon shells near the Fermi level [3].

The observed values of the spectroscopic factors for closed shell nuclei are around $S \sim 0.6$ – 0.7 [4]–[6] —yet theoretical studies appear to indicate that these values increase due to relativistic effects [7]. The small values of the spectroscopic factors are attributed to the departure from the extreme single-particle model, where the nucleon is ejected from a well defined orbit within the target nucleus.

Recent Variational Monte Carlo calculations including short-range correlations in the nuclear wave function report spectroscopic factors differing from unity only a few percent [8]–[13]. In addition, center of mass correlations can enhance the spectroscopic factor by a factor around 7% for the valence shell of ^{16}O [15, 16]. Although it has been shown that these values could be lowered by the inclusion of low-energy configuration mixing in the wave functions [14], the experimental spectroscopic factors, and hence the cross section of $(e, e'p)$ reactions for low missing energy, are not satisfactorily explained by present theoretical models.

It has been shown recently [17] that the overlap functions between the nuclear ground state with A nucleons and a residual state with $A - 1$ nucleons —which are a main ingredient in nucleon knock-out calculations, including implicitly the spectroscopic factor— can be obtained from the asymptotic behavior of the one-body density matrix (OBDM). This was confirmed in an exactly solvable many-body system in one dimension with a zero-range interaction [18]. The theorem was applied in [19] to obtain the overlap functions and spectroscopic factors from a model OBDM including Jastrow correlations, and later [20, 21] applied to the calculation of cross sections for several reactions, such as (p, d) , $(e, e'p)$ and (γ, p) . However, some problems with the numerical restoration procedure performed in [19], which is based on an exponential fit of the OBDM, were pointed out in [15], namely: i) the use of harmonic-oscillator single-particle wave functions, which do not have the correct exponential behavior in the asymptotic region, to construct the OBDM, and ii) the nature of the exponential fit allowed to obtain in [19] overlap functions for the unoccupied states, while in [15] it was demonstrated that such extraction is not possible starting from a CBF-type wave function.

In reference [21] the same restoration procedure was applied to compute overlap functions using several correlated OBDM taken from the literature. In particular, the one obtained in [22] by a truncated cluster expansion of the radial multipoles $\rho_l(r, r')$ of the OBDM. Using the above density, spectroscopic factors corresponding to the $p_{1/2}$ and $p_{3/2}$ shells of ^{16}O were reported [21] to be identical in this model and equal to 0.981. The equality of these values is probably due to the fact that the restoration procedure in [21]

started from a OBDM for $l = 1$ which (i) was not separated in spin partners $j = 1/2, 3/2$, and that (ii) was computed up to distances of $r, r' = 11$ fm, which are not large enough to separate asymptotically the two contributions $p_{1/2}$ and $p_{3/2}$. This fact, together with the problems pointed out above, makes possible that some of the effects attributed in [21] to short-range correlations, actually be a consequence of the extraction procedure of the overlap functions.

One of the motivations for this work is to clarify this situation, in particular to explore the possibility of separating the two spin-orbit partners $j = l \pm 1/2$ starting from a l -multipole of the OBDM. Note that, in the correlated model of [22], the underlying Slater determinant was built with Woods-Saxon single-particle wave functions including spin-orbit splitting, so the model can deal with different overlap functions, with different energies, corresponding to the $p_{1/2}$ and $1p_{3/2}$ shells in ^{16}O or $d_{3/2}$ and $d_{5/2}$ in ^{40}Ca .

Another aim of this paper is to perform a numerical study of the convergence of the asymptotic methods used to extract the overlap functions from the OBDM. We first carry out such study in the nuclear shell-model, where the exact overlap functions are known (they are equal to the single-particle wave functions). This allows us to determine optimum upper values of the coordinates in which one should know the OBDM in order to obtain convergence in the extraction procedure. We continue evaluating more realistic overlap functions starting from the correlated OBDM of [22], computed up to ~ 100 fm, so that we can check the convergence of the results. In particular, we will be able to obtain precise values of the spectroscopic factors for quasi-hole states.

Finally, in this work the overlap functions resulting from the above task will be inserted in a model of the $(e, e'p)$ reaction, in order to evaluate the effects of short-range correlations over nuclear response functions and cross sections. We use the DWIA model of [23, 24] which includes a new expansion of the relativistic electromagnetic current in powers of the missing momentum, but *it is not* expanded in q or ω . Combined with relativistic kinematics, this relativized model was shown in ref. [25] to give the same results as the relativistic Fermi gas for the electromagnetic inclusive responses in nuclear matter. Moreover, the present model was compared in [26] with a fully relativistic DWIA model of the reaction for $|Q^2| = 0.8$ (GeV/c) 2 , giving a reasonable description of the A_{TL} asymmetries recently measured in ^{16}O [27].

This paper is organized as follows. In sect. 2 we summarize the DWIA model we use for coincidence electron scattering, and its relation with the overlap functions, with some details of the multipole analysis of response functions placed in the appendix. In sect. 3 we present the different asymptotic procedures to extract the overlap functions from the exact OBDM, and the correlated model of the OBDM including short-range correlations of the Jastrow type. In sect. 4 we present a study of the reliability and convergence of the asymptotic methods in the shell model. The reader is directed to sect. 5 for discussion of the results obtained with the correlated model, where the effects of short-range correlations over $(e, e'p)$ observables, overlap functions, and spectroscopic factors are analyzed, with a brief application of the model to (γ, p) reactions. Finally, our conclusions are summarized in sect. 6.

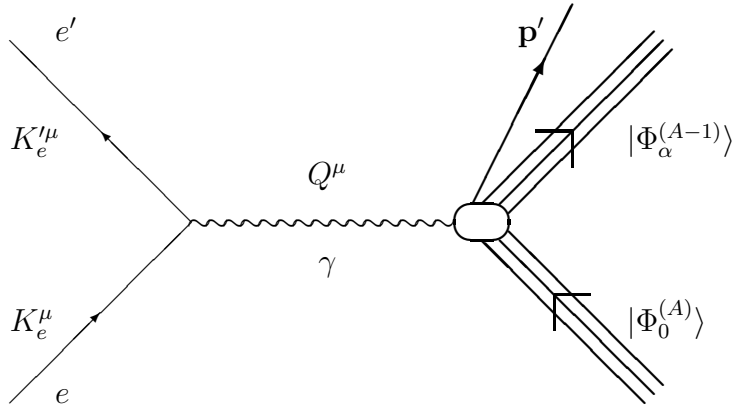


Figure 1: One-photon exchange diagram for the $(e, e'p)$ reaction.

2 DWIA model of $(e, e'p)$ reactions

2.1 Cross section and response functions

In this section we summarize those aspects of the $(e, e'p)$ reaction that are of relevance for this paper. We consider the process shown in the Feynman diagram of figure 1. Here, an incident electron with four-momentum $K_e^\mu = (\varepsilon, \mathbf{k}_e)$ interacts with a target nucleus, exchanging a virtual photon with four-momentum given by $Q^\mu = (K_e - K_e')^\mu = (\omega, \mathbf{q})$, with $K_e'^\mu = (\varepsilon', \mathbf{k}_e')$ the scattered electron four-momentum. The outgoing proton with four-momentum $P'^\mu = (E', \mathbf{p}')$ is detected in coincidence with the scattered electron.

The wave function of the spin-zero target in the ground-state is denoted $|\Phi_0^{(A)}\rangle$, with (non relativistic) energy $E_0^{(A)}$. We are interested in the low-missing energy region, where the residual nucleus is left in a bound state, $|\Phi_\alpha^{(A-1)}\rangle = |J_\alpha M_\alpha\rangle$, with (non relativistic) energy $E_\alpha^{(A-1)}$. We neglect recoil and assume parity conservation.

We work in the laboratory system, with the z -axis pointing into the \mathbf{q} -direction and the x -axis in the electron scattering plane. In this reference system, the cross section for the $(e, e'p)$ reaction, assuming plane waves and the extreme relativistic limit for the electron, can be written in the form [29]

$$\frac{d^5\sigma}{d\varepsilon' d\Omega_e' d\Omega_{p'}} = \Sigma + h\Delta \quad (1)$$

where $\Omega_{p'} = (\theta', \phi')$ are the proton emission angles, h is the electron helicity, Σ is the unpolarized cross section and Δ is the electron polarization power. These functions are given by

$$\Sigma = K\sigma_M [v_L W^L + v_T W^T + v_{TL} W^{TL} \cos \phi' + v_{TT} W^{TT} \cos 2\phi'] \quad (2)$$

$$\Delta = K\sigma_M v_{TL'} W^{TL'} \sin \phi'. \quad (3)$$

Here the kinematical factor K is proportional to the momentum p' ,

$$K = \frac{p'M}{(2\pi\hbar)^3}, \quad (4)$$

σ_M is the Mott cross section, and v_K are factors containing the dependence on the electron kinematics:

$$\begin{aligned} v_L &= \left(\frac{Q^2}{q^2}\right)^2, & v_T &= \tan^2 \frac{\theta_e}{2} - \frac{Q^2}{2q^2}, \\ v_{TL} &= \frac{Q^2}{q^2} \sqrt{\tan^2 \frac{\theta_e}{2} - \frac{Q^2}{q^2}}, & v_{TT} &= \frac{Q^2}{2q^2}, \\ v_{TL'} &= \frac{Q^2}{q^2} \tan \frac{\theta_e}{2}. \end{aligned} \quad (5)$$

Note that in this work the v_{TL} and $v_{TL'}$ variables have an extra $\sqrt{2}$ factor with respect to the corresponding definition of ref. [29].

The five exclusive nuclear response functions W^K are defined by the following linear combinations of longitudinal (L) and/or transverse (T) projections, with respect to the transfer momentum \mathbf{q} , of the relevant tensor describing the hadronic part of the emission mechanism

$$\begin{aligned} W^L &= W^{00} & W^T &= W^{xx} + W^{yy} \\ \cos \phi' W^{TL} &= W^{0x} + W^{x0} & \cos 2\phi' W^{TT} &= W^{yy} - W^{xx} \\ \sin \phi' W^{TL'} &= i(W^{0y} - W^{y0}) \end{aligned} \quad (6)$$

Here the hadronic tensor, $W^{\mu\nu}$, is related to the transition matrix elements of the nuclear electromagnetic current operator $\hat{J}^\mu(\mathbf{q})$. It is defined by

$$W^{\mu\nu} = \frac{1}{K} \sum_{m_s M_\alpha} \langle \mathbf{p}' m_s, \Phi_\alpha^{(A-1)} | \hat{J}^\mu(\mathbf{q}) | \Phi_0^{(A)} \rangle \langle \mathbf{p}' m_s, \Phi_\alpha^{(A-1)} | \hat{J}^\nu(\mathbf{q}) | \Phi_0^{(A)} \rangle \quad (7)$$

and it represents the maximum information that can be obtained in these kinds of experiments. Note that the dependence on the azimuthal angle of the emitted proton, ϕ' , is given explicitly in Eqs. (6). The final hadronic states entering in the definition of the hadronic tensor, $|\mathbf{p}' m_s, \Phi_\alpha^{(A-1)}\rangle$ are in principle the exact scattering states with the corresponding boundary conditions, i.e., they correspond asymptotically to a nucleon with momentum \mathbf{p}' and third spin component m_s , and a daughter nucleus in the state $|\Phi_\alpha^{(A-1)}\rangle$.

2.2 DWIA and overlap functions

In this paper we consider a DWIA model of the current matrix elements between hadronic states that enter into the hadronic tensor (7). This model is based in the impulse approximation, in which we assume that the nuclear electromagnetic current is a one-body operator. Hence we are neglecting two-body contributions coming mainly from meson-exchange currents. The contribution from these two-body currents was analyzed in [30]. However, in this work we are not including that contribution, since we are interested in studying the genuine short-range correlation effects.

The impulse approximation current operator can be written in momentum space as

$$\hat{J}^\mu(\mathbf{q}) = \int d^3k J^\mu(\mathbf{q} + \mathbf{k}, \mathbf{k}) a_{\mathbf{q}+\mathbf{k}}^\dagger a_{\mathbf{k}}. \quad (8)$$

where $J^\mu(\mathbf{q} + \mathbf{k}, \mathbf{k})$ is the single-nucleon current for which we use a new non-relativistic expansion to first order in \mathbf{k}/M , first proposed in refs. [25, 31]. The time component of this current contains charge and spin-orbit contributions, while the transverse current is given as the sum of magnetization plus convection pieces. However, each piece of the current differs from the traditional non-relativistic one, containing, in addition to the nucleon form factors, relativistic correction factors which depend on q and ω . In ref. [25] it was shown that, beginning with the usual non-relativistic Fermi gas and using relativistic kinematics plus the new currents, the same longitudinal and transverse inclusive response functions are obtained essentially as in the relativistic Fermi gas model for arbitrary values of q , which can be bigger than 1 GeV. Note that the usual non-relativistic forms of the current, that are also expanded in powers of q/M , begin to fail for high values of $q > 500$ MeV/ c and cannot be applied for $q \sim M$.

The second approximation used in DWIA is the description of the ejected proton state as a single-particle wave function $\chi_{\mathbf{p}'}(\mathbf{r})$, obtained as the solution of the Schrödinger equation with a complex optical potential fitted to elastic-scattering data. The final hadronic state is then written as

$$|\Phi_\alpha^{(A-1)}, \chi_{\mathbf{p}'}\rangle = \int d^3k \tilde{\chi}_{\mathbf{p}'}(\mathbf{k}) a_{\mathbf{k}}^\dagger |\Phi_\alpha^{(A-1)}\rangle \quad (9)$$

where $\int d^3k \tilde{\chi}_{\mathbf{p}'}(\mathbf{k}) a_{\mathbf{k}}^\dagger$ is the field operator creating a nucleon in the state $\tilde{\chi}_{\mathbf{p}'}(\mathbf{k})$, i.e., the wave function of the ejected proton in momentum space. From here we can write the matrix element of the current (8) as

$$\langle \Phi_\alpha^{(A-1)}, \chi_{\mathbf{p}'} | \hat{J}^\mu(\mathbf{q}) | \Phi_0^{(A)} \rangle = \int d^3k d^3k' \tilde{\chi}_{\mathbf{p}'}^*(\mathbf{k}') J^\mu(\mathbf{q} + \mathbf{k}, \mathbf{k}) \langle \Phi_\alpha^{(A-1)} | a_{\mathbf{k}'} a_{\mathbf{q}+\mathbf{k}}^\dagger a_{\mathbf{k}} | \Phi_0^{(A)} \rangle \quad (10)$$

Now we use the anti-commutation rules of the Fermion operators

$$a_{\mathbf{k}'} a_{\mathbf{q}+\mathbf{k}}^\dagger = \delta(\mathbf{k}' - \mathbf{q} - \mathbf{k}) - a_{\mathbf{q}+\mathbf{k}}^\dagger a_{\mathbf{k}'}. \quad (11)$$

The contribution of the second term in this equation, $a_{\mathbf{q}+\mathbf{k}}^\dagger a_{\mathbf{k}'}$, can be neglected if

1. the momentum of the ejected proton is much larger than the Fermi momentum of the initial nucleus, $p' \gg p_F$, this condition is usually fulfilled in the experiments, and
2. the wave function $\tilde{\chi}_{\mathbf{p}'}(\mathbf{k}')$ of the ejected nucleon is negligible outside of an interval of momentum $\Delta\mathbf{k}'$ around the central value \mathbf{p}' .

In such cases, we can write

$$\tilde{\chi}_{\mathbf{p}'}^*(\mathbf{k}')a_{\mathbf{k}'}|\Phi_0^{(A)}\rangle \simeq 0. \quad (12)$$

This condition is equivalent to assume that the wave function $\tilde{\chi}_{\mathbf{p}'}$ is orthogonal to the components of the initial state. Non-orthogonality effects have been found to be small in the region of low missing momentum. However, the assumptions done in this approximation are not valid for high missing momentum, for which the region neglected by the approximation (12) is explored.

We are interested here in the low missing momentum region so we can write the current matrix element as

$$\langle\Phi_\alpha^{(A-1)}, \chi_{\mathbf{p}'}|\hat{J}^\mu(\mathbf{q})|\Phi_0^{(A)}\rangle = \int d^3k \tilde{\chi}_{\mathbf{p}'}^*(\mathbf{k} + \mathbf{q})J^\mu(\mathbf{q} + \mathbf{k}, \mathbf{k})\langle\Phi_\alpha^{(A-1)}|a_{\mathbf{k}}|\Phi_0^{(A)}\rangle, \quad (13)$$

In this equation we identify the single-particle overlap function between the states $\Phi_0^{(A)}$ and $\Phi_\alpha^{(A-1)}$, defined, in momentum space, as the matrix element [1]

$$\tilde{\Psi}_\alpha(\mathbf{k}) = \langle\Phi_\alpha^{(A-1)}|a_{\mathbf{k}}|\Phi_0^{(A)}\rangle. \quad (14)$$

Using this definition, we can write the many-body matrix element of the current (13) as a matrix element between single-particle states, namely between the overlap function and the distorted wave of the final proton

$$\langle\Phi_\alpha^{(A-1)}, \chi_{\mathbf{p}'}|\hat{J}^\mu(\mathbf{q})|\Phi_0^{(A)}\rangle = \langle\chi_{\mathbf{p}'}|J^\mu(\mathbf{q})|\Psi_\alpha\rangle. \quad (15)$$

This is the matrix element that we compute in the present work in order to obtain the $(e, e'p)$ response functions. The information about short-range correlations is contained inside the overlap functions Ψ_α , which are obtained from a correlated OBDM by the asymptotic method explained in the next section. The matrix elements (15) are computed by performing a multipole expansion of the current operators in terms of Coulomb, electric and magnetic operators, and of the outgoing wave function $\chi_{\mathbf{p}'}$ in partial waves. The corresponding response functions (6) are expanded in Legendre functions of $\cos\theta'$ (the angle between \mathbf{p}' and \mathbf{q}), and their expressions are given in appendix A.

The physical interpretation of the overlap function is clear by writing it in the form

$$\tilde{\Psi}_\alpha(\mathbf{k}) = \sqrt{S_\alpha}\phi_\alpha(\mathbf{k}) \quad (16)$$

where ϕ_α is the overlap function normalized to the unity, and it is usually identified with the effective single-particle wave function of the “shell” occupied by the ejected nucleon. The spectroscopic factor $S_\alpha = \langle \Psi_\alpha | \Psi_\alpha \rangle$ is the occupancy probability of the shell.

The plane wave impulse approximation (PWIA) will be useful for the physical interpretation of the correlation effects shown below in terms of overlap functions. In PWIA since FSI is neglected, the wave function of the ejected proton is a plane wave, $\tilde{\chi}_{\mathbf{p}'}(\mathbf{k}) = \delta(\mathbf{k} - \mathbf{p}')$, and hence eq. (13) becomes

$$\langle \Phi_\alpha^{(A-1)}, \chi_{\mathbf{p}'} | \hat{J}^\mu(\mathbf{q}) | \Phi_0^{(A)} \rangle = J^\mu(\mathbf{p}', \mathbf{p}) \tilde{\Psi}_\alpha(\mathbf{p}), \quad (17)$$

where we have introduced the missing momentum, $\mathbf{p} \equiv \mathbf{p}' - \mathbf{q}$, identified with the momentum of the proton before the interaction. As a consequence of the above factorization property, the hadronic tensor (7) is proportional to the momentum distribution $|\tilde{\Psi}_\alpha(\mathbf{p})|^2$ of the overlap function

$$W^{\mu\nu} = w^{\mu\nu}(\mathbf{p}', \mathbf{p}) \left| \tilde{\Psi}_\alpha(\mathbf{p}) \right|^2, \quad (18)$$

where $w^{\mu\nu}(\mathbf{p}', \mathbf{p})$ is the hadronic tensor for a single nucleon with initial momentum \mathbf{p} and final momentum \mathbf{p}' :

$$w^{\mu\nu}(\mathbf{p}', \mathbf{p}) = J^\mu(\mathbf{p}', \mathbf{p})^* J^\nu(\mathbf{p}', \mathbf{p}). \quad (19)$$

In the same way, the response functions are also proportional to the momentum distribution:

$$W^K = w^K(\mathbf{p}', \mathbf{p}) \left| \tilde{\Psi}_\alpha(\mathbf{p}) \right|^2 \quad (20)$$

where $w^K(\mathbf{p}', \mathbf{p})$ are the response functions for electron scattering by a single proton with momentum \mathbf{p} .

When the FSI is turned on, the above factorization is not true anymore but the general behavior of the response functions is preserved. The mean effect of the FSI is a reduction of the responses due to the absorptive part of the optical potential. We will see below that the effects of the short-range correlations are decoupled from the FSI effects.

3 Correlated model of OBDM and overlap functions

3.1 Overlap functions

The basic quantities of interest for our calculations are the overlap functions between nuclear states with A and $A - 1$ nucleons, eq. (14). We work in coordinate space, where the overlap function is

$$\Psi_\alpha(x) = \langle \Phi_\alpha^{(A-1)} | a(x) | \Phi_0^{(A)} \rangle. \quad (21)$$

Here $x = (\mathbf{r}, s_z, t_z)$ is a generalized coordinate including spin and isospin, \mathbf{r} is the relative coordinate respect to the center of mass of the residual nucleus $\Phi_f^{(A-1)}$, and $a(x)$ is the destruction operator of a nucleon at the point x . We assume that the initial nucleus is in the ground state $\Phi_0^{(A)}$ with energy $E_0^{(A)}$, while the residual nucleus remains in an arbitrary state $\Phi_\alpha^{(A-1)}$, with energy $E_\alpha^{(A-1)}$.

Using the Schrödinger equation verified by the initial and final nuclear states, a system of integro-differential equations for the overlap functions can be written [28]. However in the procedure explained below to compute these functions for the low-energy levels of the residual nucleus we only make use of its asymptotic behavior, which is based on the following equation verified by the overlap functions at large distances, $r \rightarrow \infty$

$$-\frac{\hbar^2}{2\mu}\nabla^2\Psi_\alpha(\mathbf{r}) + (A-1)v(\mathbf{r})\Psi_\alpha(\mathbf{r}) = [E_0^{(A)} - E_\alpha^{(A-1)}]\Psi_\alpha(\mathbf{r}) \quad (22)$$

where $v(\mathbf{r})$ is the NN potential and $\mathbf{r} = \mathbf{r}_1 - \mathbf{r}_2$ is the relative coordinate. This equation means that the overlap function behaves asymptotically as a single-particle interacting with the $A-1$ nucleons of the residual system as if they were located at the same position, namely at the center of mass of the residual nucleus. Of course this is only valid for so large distances that it is not possible to take notice of the small separation distances of nucleons within the nucleus.

In the cases when the initial nucleus has spin zero and the parity of nuclear states is a good quantum number, it is possible to separate the overlap function in radial and spin-angular parts [28]

$$\Psi_\alpha(\mathbf{r}) = \phi_{nlj}(r)\mathcal{Y}_{ljm}(\theta, \phi). \quad (23)$$

with $j = J_\alpha$ the spin of the final nuclear state $\Phi_\alpha^{(A-1)}$, and $l = j \pm 1/2$, depending on the parity of this state. The radial overlap function $\phi_{nlj}(r)$ (where the quantum number n is reminiscent of the later identification with shell-model states) verifies for large distances a radial equation coming from eq. (22), with an asymptotic eigenvalue given as the difference between the energies of the initial and residual nuclei $E_0^{(A)} - E_\alpha^{(A-1)}$, which is a negative number for every value of the excitation energy of the residual nucleus. Therefore the overlap function behaves as a bound state and it has the typical exponential decay

$$\phi_{nlj}(r) \sim C \frac{e^{-kr}}{r}, \quad r \rightarrow \infty \quad (24)$$

with

$$k = \sqrt{\frac{2\mu |E_\alpha^{(A-1)} - E_0^{(A)}|}{\hbar^2}}. \quad (25)$$

The exponential decay is modified by a logarithmic phase in the case of proton emission, where the Coulomb potential plays a role. However this fact does not modify the following results.

The relation between the overlap functions and the OBDM follows from the definition of the density matrix of the initial nucleus:

$$\rho(\mathbf{r}_1, \mathbf{r}_2) = \sum_s \langle \Phi_0^{(A)} | a^\dagger(\mathbf{r}_1, s) a(\mathbf{r}_2, s) | \Phi_0^{(A)} \rangle \quad (26)$$

Inserting a complete set of states $|\Phi_\alpha^{(A-1)}\rangle$ of the residual nucleus between the two Fermi operators we obtain an expansion of the OBDM in terms of overlap functions

$$\rho(\mathbf{r}_1, \mathbf{r}_2) = \sum_\alpha \Psi_\alpha^\dagger(\mathbf{r}_1) \Psi_\alpha(\mathbf{r}_2) \quad (27)$$

In this work we consider the OBDM expanded in multipole densities with angular momentum l

$$\rho(\mathbf{r}_1, \mathbf{r}_2) = \frac{1}{4\pi} \sum_l \rho_l(r_1, r_2) P_l(\cos \theta_{12}) \quad (28)$$

where θ_{12} is the angle between \mathbf{r}_1 and \mathbf{r}_2 . Inserting the expression (23) into (27) and performing the sums over third components we find the corresponding expansion of the OBDM multipoles in terms of radial overlap functions

$$\rho_l(r_1, r_2) = \sum_{nj} (2j+1) \phi_{nlj}(r_1) \phi_{nlj}(r_2) = \sum_{nj} \psi_{nlj}(r_1) \psi_{nlj}(r_2) \quad (29)$$

where we have defined $\psi_{nlj}(r)$ as the radial part of the overlap function normalized with a factor $\sqrt{2j+1}$.

$$\psi_{nlj}(r) = \sqrt{2j+1} \phi_{nlj}(r). \quad (30)$$

3.2 Asymptotic methods for computing the overlap functions

We recall here the method presented in [17] to compute the overlap functions by means of the exact OBDM for the ground state of the A -particle system.

We consider a fixed value of l , and denote the corresponding radial overlap functions with angular momentum l simply as $\psi_\alpha(r)$, $\alpha = 0, 1, 2, \dots$, corresponding to bound states of the residual nucleus ordered by increasing energy $E_0^{(A-1)} < E_1^{(A-1)} < \dots$, and with asymptotic behavior

$$\psi_\alpha(a) \sim C_\alpha \frac{e^{-k_\alpha a}}{a}, \quad a \rightarrow \infty \quad (31)$$

with $k_\alpha = [2\mu(E_\alpha^{(A-1)} - E_0^{(A)})]^{1/2}/\hbar$.

The asymptotic behavior of the OBDM is, from eq. (29),

$$\rho_l(r, a) \sim \sum_\alpha \psi_\alpha(r) C_\alpha \frac{e^{-k_\alpha a}}{a}, \quad a \rightarrow \infty. \quad (32)$$

Now, due to the ordering $k_0 < k_1 < \dots$, the above sum is dominated by the first term, with the slowest exponential decay, for long distances a such that $a(k_1 - k_0) \gg 1$

$$\rho_l(r, a) \sim \psi_0(r) C_0 \frac{e^{-k_0 a}}{a}, \quad a \rightarrow \infty \quad (33)$$

Combining this equation with the asymptotic behavior of the diagonal part, which allows us to determine the constant C_0 ,

$$\rho_l(a, a) \sim |C_0|^2 \frac{e^{-2k_0 a}}{a^2}, \quad a \rightarrow \infty, \quad (34)$$

we can compute the overlap function $\psi_0(r)$ and the corresponding separation energy. In order to obtain the second overlap function, we apply the procedure to the density obtained subtracting the contribution of the first overlap

$$\rho_l(r, a) - \psi_0(r)\psi_0(a) \sim \psi_1(r) C_1 \frac{e^{-k_1 a}}{a}, \quad a \rightarrow \infty. \quad (35)$$

In principle all the overlap functions corresponding to bound states of the residual nucleus may be obtained by repeating these steps. In the next section we check the validity of this procedure, which in the present paper we call “exponential decay method”.

There is an alternative, equivalent way [15] of obtaining the overlap functions from the asymptotic behavior of the OBDM, without using explicitly the exponential decay property. We will illustrate it using the fact that the diagonal part of the OBDM has also an exponential decay given by eq. (34), from where we can write

$$\sqrt{\rho_l(a, a)} \sim |C_0| \frac{e^{-k_0 a}}{a}, \quad a \rightarrow \infty, \quad (36)$$

which is precisely the behavior of the first overlap function, eq. (31). Using this equation in the asymptotic form of the OBDM, we obtain

$$\psi_0(r) = \lim_{a \rightarrow \infty} \frac{\rho_l(r, a)}{\sqrt{\rho_l(a, a)}}. \quad (37)$$

Note that in the case $C_0 < 0$ we obtain a minus sign which is just a global phase that can be inserted in the overlap function. The application of this expression, which we call “ $\sqrt{\rho}$ -method”, has clear advantages over the exponential decay one when it is used to compute the overlap functions from a model OBDM without the correct asymptotic behavior (for instance, constructed with harmonic oscillator single-particle wave functions).

3.3 Model of correlated OBDM

In this work we compute the overlap functions of closed shell nuclei by applying the last method explained to a correlated OBDM. We use the model of ref. [22] which includes

short-range correlations up to first order in a cluster expansion of the OBDM. The density and momentum distributions were compared with the FHNC calculation of ref. [32], with a good agreement between both models.

We begin with the OBDM of the initial nucleus $|\Phi_0^{(A)}\rangle$, written as

$$\rho(x_1, x_2) = \frac{A}{\langle \Phi_0^{(A)} | \Phi_0^{(A)} \rangle} \int dx_2, \dots, dx_A \Phi_0^{(A)*}(x_1, \dots, x_A) \Phi_0^{(A)}(x_1, \dots, x_A) \quad (38)$$

For the applications to $(e, e'p)$ reactions, we will only need the proton density, this is obtained inserting in the previous equation the projection operator $Q(1) = \frac{1}{2}(1 + \tau_z(1))$.

Short-range correlations are introduced within the model by the Jastrow ansatz for the nuclear wave function

$$\Phi_0^{(A)}(1, 2, \dots, A) = F(1, 2, \dots, A) \Phi_{Sl}^{(A)}(1, 2, \dots, A). \quad (39)$$

Here $\Phi_{Sl}^{(A)}$ is a Slater determinant and F is a correlation function containing two-body central correlations

$$F(1, \dots, A) = \prod_{i>j=1}^A f(r_{ij}), \quad (40)$$

where $r_{ij} = |\mathbf{r}_i - \mathbf{r}_j|$, and the function $f(r_{ij})$ has a Gaussian functional dependence

$$f(r) = 1 - A \exp(-Br^2) \quad (41)$$

We use the parameters $A = 0.7$ and $B = 2.2 \text{ fm}^{-2}$ which were fixed in [32] by minimizing the nuclear binding energies for the Afnan and Tang S3 interaction. In ref. [22] up to six spin-isospin correlation channels were included. However, the numerical effort grows in the present case, since we have computed the OBDM up to distances so large as 100 fm, essential to separate the first overlap function in some cases. This fact compelled us to reduce the number of correlation channels and to use a Gaussian dependence, in order to perform analytically the multipole expansion of the correlation function $f(r)$.

The OBDM is calculated by a cluster expansion, writing the correlation function as

$$F(1, \dots, A) = 1 + \prod_{i>j} h(r_{ij}) \quad (42)$$

and performing an expansion up to second order in h . The resulting OBDM for protons can then be written as

$$\begin{aligned} \rho_1^p(\mathbf{r}_1, \mathbf{r}'_1) &= \rho_0^p(\mathbf{r}_1, \mathbf{r}'_1) + A(\mathbf{r}_1, \mathbf{r}'_1) - B(\mathbf{r}_1, \mathbf{r}'_1) - C(\mathbf{r}_1, \mathbf{r}'_1) + D(\mathbf{r}_1, \mathbf{r}'_1) \\ &= \rho_0^p(\mathbf{r}_1, \mathbf{r}'_1) + \rho_0(\mathbf{r}_1, \mathbf{r}'_1) \int d^3r_2 H(\mathbf{r}_1, \mathbf{r}'_1, \mathbf{r}_2) \rho_0(\mathbf{r}_2, \mathbf{r}_2) \\ &\quad - \int d^3r_2 \rho_0(\mathbf{r}_1, \mathbf{r}_2) H(\mathbf{r}_1, \mathbf{r}'_1, \mathbf{r}_2) \rho_0(\mathbf{r}_2, \mathbf{r}'_1) \\ &\quad - \int d^3r_2 \int d^3r_3 \rho_0(\mathbf{r}_1, \mathbf{r}_2) \rho_0(\mathbf{r}_2, \mathbf{r}'_1) \rho_0(\mathbf{r}_3, \mathbf{r}_3) H(\mathbf{r}_2, \mathbf{r}_2, \mathbf{r}_3) \\ &\quad + \int d^3r_2 \int d^3r_3 \rho_0(\mathbf{r}_1, \mathbf{r}_2) \rho_0(\mathbf{r}_2, \mathbf{r}_3) \rho_0(\mathbf{r}_3, \mathbf{r}'_1) H(\mathbf{r}_2, \mathbf{r}_2, \mathbf{r}_3) \end{aligned} \quad (43)$$

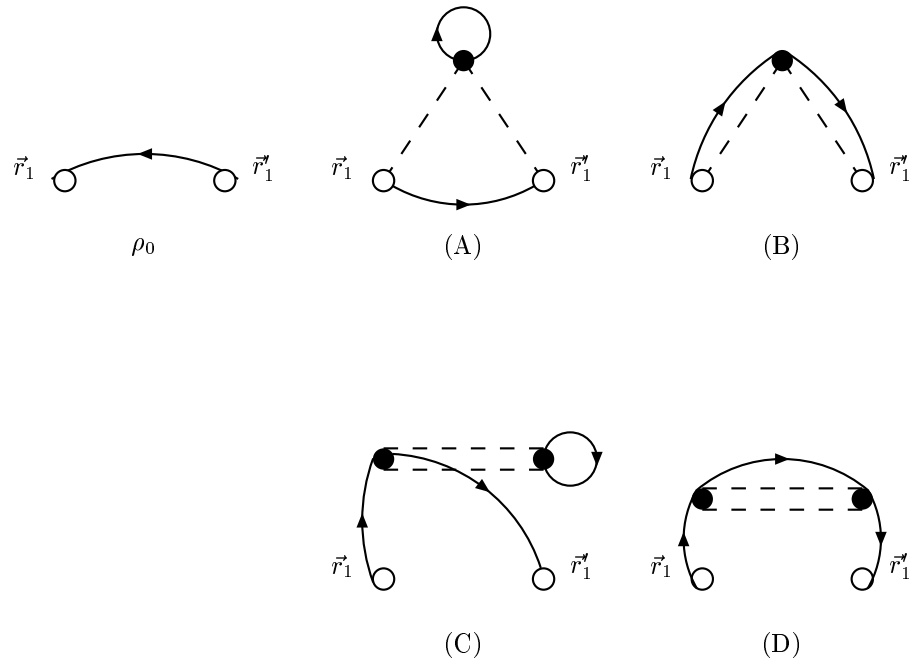


Figure 2: Diagrams considered in the cluster expansion of the OBDM. The dashed lines indicate the dynamical correlations $f(r_{ij})$ and the solid lines the uncorrelated density.

where the new correlation function H can be expressed in terms of the correlation function $f(r)$

$$H(\mathbf{r}_i, \mathbf{r}_j, \mathbf{r}_k) = Q(1)[f(r_{ik})f(r_{jk}) - 1]. \quad (44)$$

This function contains the correlations between the two pairs of particles (ik) and (jk) . The operator $Q(1)$ guarantees that the particle 1 is a proton.

The functions A, B, C, D corresponding to the corrections to the uncorrelated OBDM, $\rho^0(\mathbf{r}_1, \mathbf{r}'_1)$, are represented diagrammatically in Fig. 2. Therein, the open circles represent the two coordinates \mathbf{r}_1 and \mathbf{r}'_1 , while the solid dots refer to coordinates of inner nucleons which are correlated to the rest. A continuous line represents a non correlated OBDM $\rho_0(\mathbf{r}_1, \mathbf{r}_2)$, while the dashed lines joins the different particles involved in the new correlation function H . Thus in the diagrams A and B , the particles 1 and 1' are simultaneously correlated to a third particle 2. On the other hand, in diagrams C and D there are two inner particles 2 and 3 which are correlated between them.

Using the above expression a multipole expansion is performed to obtain the radial densities, $\rho_l(r, r')$, needed to compute the overlap functions for different angular momenta. We refer to [22] for details on this expansion. Note that, on the contrary to ref. [15], in this model we do not separate the multipoles $\rho_{lj}(r, r')$ of the density in spin-orbit partners $j = l \pm 1/2$ explicitly. However these two contributions are included in ρ_l . Since our correlated OBDM is based in a single-particle basis obtained with a Woods-Saxon potential including spin-orbit interaction, the two overlap functions ψ_{nlj} corresponding to an occupied shell have different energies from the beginning and, in principle, they can be separated in the asymptotic region.

4 Test of the asymptotic methods in the shell model

Before computing the overlap functions using the correlated model of sect. 3.3, it is convenient to perform a test of the asymptotic methods using a nuclear model where the exact solution is known *a priori*. In this way we will be able to determine (i) which of the algorithms introduced below is more adequate to extract the overlap functions, and (ii) the asymptotic distance needed to separate the several overlap functions.

We perform this analysis in the extreme shell model (SM), where the overlap functions are just the single-particle wave functions of the occupied shells. Apart from its simplicity, another reason to choose the SM is that corresponds to the zero-order of the correlated model. Under the assumption that the Jastrow correlations, as a first-order correction to the SM, do not drastically change the asymptotic behavior of the OBDM, we expect that the convergence conditions found in the SM will keep valid in the correlated model.

The single-particle wave functions in the SM are obtained by solving the Schrödinger equation for a nucleon in a Woods-Saxon potential

$$V_{WS}(r) = -\frac{V_0}{1 + \exp(\frac{r-R}{a_0})} - \vec{l} \cdot \vec{\sigma} \left(\frac{\hbar}{m_\pi c} \right)^2 \frac{1}{r} \frac{d}{dr} \left[\frac{V_{ls}}{1 + \exp(\frac{r-R}{a_{ls}})} \right] + V_C(r), \quad (45)$$

Nucleus		V_0 [Mev]	V_{ls} [Mev]	R [fm]	a_0 [fm]	a_{ls} [fm]
^{12}C	P	62.00	3.20	2.74	0.57	0.57
	N	60.00	3.15	2.74	0.57	0.57
^{16}O	P	52.50	7.00	3.02	0.53	0.53
	N	52.50	6.54	3.02	0.53	0.53
^{40}Ca	P	57.50	11.11	4.10	0.53	0.53
	N	55.00	8.50	4.10	0.53	0.53
^{48}Ca	P	59.50	8.37	4.36	0.53	0.53
	N	50.00	7.54	4.36	0.53	0.53

Table 1: Parameters of the Woods-Saxon potential.

where $V_C(r)$ is the Coulomb potential for protons, of an uniform charge distribution with radius R . The parameters of the potential are given in table 1 for the closed shell nuclei considered in this work.

We have solved numerically the radial equation up to distances of $r = 100$ fm, in order to compute the corresponding OBDM in a wide asymptotic region, where we will be able to check the convergence of the methods. First, we compared our wave functions with the ones obtained integrating the equation up to 11 fm, as is done traditionally, obtaining essentially the same answer in both cases up to the region close to $r \sim 11$ fm. The energy eigenvalues of the proton shells are shown in the third column of table 2. For each value of l , we construct the shell model OBDM as a sum of the corresponding single-particle radial densities of the occupied states with angular momentum equal to l .

4.1 Exponential decay methods.

We first focus on the asymptotic decay method, in which the overlap functions are obtained by fitting the exponential decay of the OBDM, eq. (33). This can be done in several ways:

- (I) **Logarithm fit.** Taking the logarithm in both sides of eqs. (33,34) we have asymptotically,

$$\ln\{a|\rho_l(r, a)|\} = \ln\{C_0|\psi_0(r)|\} - k_0a \quad (46)$$

$$\ln\{a^2\rho_l(a, a)\} = \ln C_0^2 - 2k_0a. \quad (47)$$

We first compute C_0 by fitting a straight line to $\ln\{a^2\rho_l(a, a)\}$ (we assume $C_0 > 0$ since this is just a global phase). Then $|\psi_0(r)|$ is computed by fitting another straight line to $\ln\{a|\rho_l(r, a)|\}$ and dividing by C_0 . Finally, the sign of $\psi_0(r)$ is obtained from eq. (33) as the one of $\rho_l(r, a)$.

Nucleus	nlj	$ E_{ws} $ [Mev]
^{12}C	$1s_{1/2}$	32.27
	$1p_{3/2}$	15.49
^{16}O	$1s_{1/2}$	27.36
	$1p_{3/2}$	13.92
	$1p_{1/2}$	9.29
^{40}Ca	$1s_{1/2}$	35.54
	$2s_{1/2}$	9.80
	$1p_{3/2}$	26.12
	$1p_{1/2}$	22.63
	$1d_{5/2}$	15.83
	$1d_{3/2}$	8.37
^{48}Ca	$1s_{1/2}$	39.25
	$2s_{1/2}$	14.73
	$1p_{3/2}$	30.15
	$1p_{1/2}$	28.00
	$1d_{5/2}$	19.92
	$1d_{3/2}$	15.14

Table 2: Energies of the proton single particles in the shell model, E_{WS} .

- (II) **Trace minimization.** The overlap function is calculated dividing the OBDM by an exponential

$$\psi_0(r) = \frac{\rho_l(r, a)}{C_0 \frac{e^{-k_0 a}}{a}} \quad (48)$$

with C_0 and k_0 determined from the diagonal part $\rho_l(a, a)$ as in method I. The remaining parameter, a , is chosen by imposing that the overlap density $\rho_l^0(r, r') = \psi_0(r)\psi_0(r')$ be as close as possible to the OBDM, $\rho_l(r, r')$, for every value of r and r' contained in an asymptotic interval $[a_l, a_u]$. This condition is achieved by minimizing the trace functional

$$F(a) \equiv \text{Tr}[\rho_l - \rho_l^0] = \int_0^{a_u} dr \int_{a_l}^{a_u} dr' \left[\rho_l(r, r') - \frac{\rho_l(r, a)\rho_l(r', a)}{C_0^2 \frac{\exp(-2k_0 a)}{a^2}} \right]^2 \quad (49)$$

- (III) **Trace minimization with three parameters.** This third method is a variation of fit II, that considers C_0 and k_0 as additional parameters in the trace functional. So the three parameters are now fixed by computing the absolute minimum of this functional.

The fit procedure II is similar to the one applied in ref. [19]. In the following we compare the results provided by these methods for different choices of the asymptotic

interval $[a_l, a_u]$ where the fit is performed. We shall study the case of ^{40}Ca in the shell model, where the OBDM contains $l = 0, 1, 2$ multipoles.

In Fig. 3 we show results for $l = 0$, corresponding to the overlap functions of the shells $2s_{1/2}$ (first overlap function) and $1s_{1/2}$ (second overlap). Panel (a) shows an example of what is obtained using a OBDM computed up to $a_u = 11$ fm. In addition we have used $a_l = 2.3$ fm, which is the point where the density $\rho_0(r, r)$ reaches the 10% of its maximum. This value is not large enough to be considered asymptotic and the resulting overlap functions are clearly incorrect. In this figure we note a misbehavior of fit I (dashed lines) in the region close to the node, where eq. (33) is not valid, since the OBDM is dominated there by the *second* overlap function. This misbehavior is not found in fits II (dot-dashed lines) and III (dotted lines) because in both cases the exponential fit is done globally and not point by point. Since the first overlap has not been adequately extracted, we also obtain an incorrect result for the second overlap, shown in panel (b). We note in this panel that the displayed curves stop around 2–2.5 fm. The reason is that the subtracted diagonal part $\rho_0(r, r) - \phi_0(r)^2$ becomes negative in this region as a consequence of the incorrect value of $\phi_0(r)$.

The results for the first overlap function improve when we increase a_u to 15 fm and a_l to 5.9 fm, corresponding this last distance to the point where the density is 1% of its maximum value, as it is shown in panel (c). Even though there is a clear improvement with respect to the results of panel (a), there is still a small difference with respect to the exact result (solid line), which is larger for the results of fit I. These small differences are amplified when the second overlap function, shown in panel (d), is computed. Nevertheless there is also a clear improvement respect to the former results of (b).

In order to find a reasonable agreement with the exact result we have to use $a_l = 13.7$ fm, where the density reaches the $10^{-7}\%$ of its maximum value. The corresponding results are shown in panel (e), where we have used again $a_u = 15$ fm. Although not seen in the scale of the figure, the results of fits II and III are closer to the exact result than the corresponding to fit I. Finally, the second overlap function is shown in panel (f), where we still note small differences with the exact result specially for low r . The results for the second overlap rely heavily on the adequacy of the computed first overlap function. These small differences can be further minimized if a higher value for the asymptotic points a_l, a_u is utilized in computing the first overlap. We will see this when we discuss the $\sqrt{\rho}$ method.

In the case of the second overlap for $l = 0$ we use a different interval $[a'_l, a'_u]$ from the one considered in the corresponding first overlap. The upper limit a'_u is chosen as the point where the subtracted density $\rho_0(r, r) - \psi_0(r)^2$ becomes negative, since this is a clear indication that the first overlap is incorrect at this point. The lower limit a'_l is chosen as the point where the subtracted density is 10% of its maximum value. This value is not critical in the cases in which the first overlap function is incorrect, as there is no improvement by changing a'_l . On the other hand, in the cases in which we obtain a reasonable result for the first overlap function, the result for the second one is already

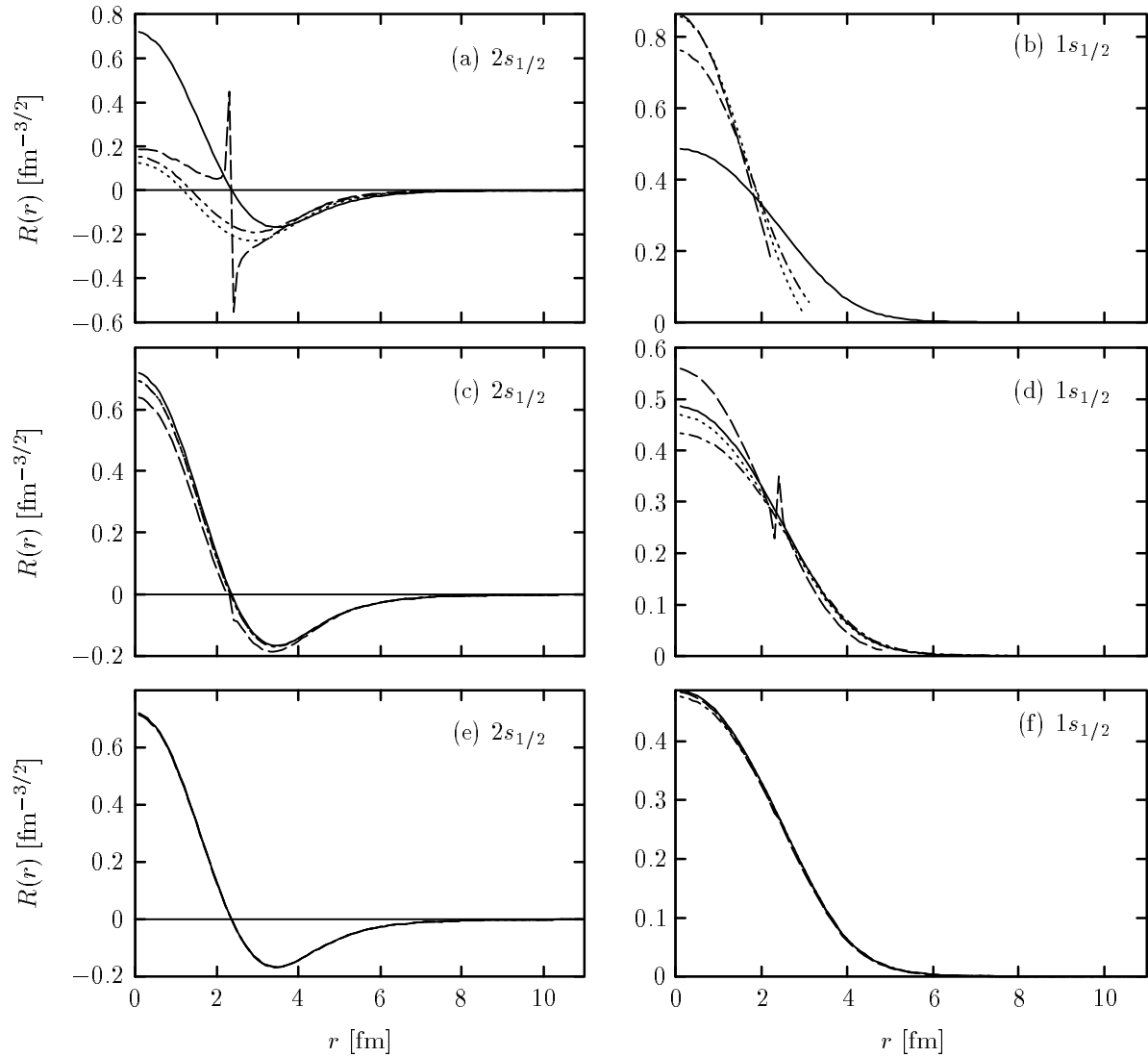


Figure 3: Overlap functions of ^{40}Ca for $l = 0$ in shell model, computed with the exponential decay method I (dashed lines), II (dot-dashed lines) and III (dotted lines). With solid lines we show the radial functions, corresponding to the exact result. The several panels refer to different asymptotic intervals $[a_l, a_u]$ considered in the fit of the first overlap function, namely $[2.3 \text{ fm}, 11 \text{ fm}]$ for (a,b), $[5.9 \text{ fm}, 15 \text{ fm}]$ for (c,d), and $[13.7 \text{ fm}, 15 \text{ fm}]$ for (e,f).

quite good for low values of a'_l . This is a consequence of the simplicity of the shell model where we are working since in this case the subtracted density is factorizable as a product of single-particle wave functions of the $1s_{1/2}$ shell

$$\rho_0(r, r') - \psi_0(r)\psi_0(r') = 2R_{1s_{1/2}}(r)R_{1s_{1/2}}(r'). \quad (50)$$

and it is not necessary to separate a third overlap function. Of course in the correlated case, where there are extra contributions to the OBDM, one should be careful and choose a value of a'_l for which there is convergence.

In Fig. 4 we show the first overlap functions of ^{40}Ca for $l = 1, 2$, corresponding to the shells $1p_{1/2}$ (a) and $1d_{3/2}$ (b). The exact results are shown with solid lines, while with dashed, dot-dashed and dotted lines we show respectively the results of the fit II performed for three different asymptotic intervals with upper limits $a_u = 11, 15$ and 20 fm, and lower limits corresponding to the points where the OBDM reaches the 10%, 0.1% and $10^{-9}\%$ of its maximum value. In panel (a), corresponding to the $1p_{1/2}$ shell, the three fits give a similar result which is around a factor of two higher than the exact answer. The results do not show a noticeable improvement when the asymptotic interval is increased from $[5.9, 15]$ fm to $[13, 20]$ fm. In panel (b), the results of fit II corresponding to the $1d_{3/2}$ shell are again above the exact answer, although we note a convergence trend in going from the interval $[6.6, 15]$ (dot-dashed) to $[17.2, 20]$ fm (dotted). The results obtained with fits I and III are not shown in the figure; fit III gives essentially the same result as fit II, while fit I is worse than fit II.

It is clear from these results, that it is not possible to extract the first overlap function for the p and d shells, using asymptotic distances up to 20 fm. This is related to the fact that the energies of the spin-orbit partners ($1p_{1/2}$, $1p_{3/2}$), and ($1d_{3/2}$, $1d_{5/2}$) have close values, their difference being around 3.5 MeV and 7.5 MeV respectively (see table 2). Hence, at 20 fm the contribution of the second overlap function is still important (see panels (e)–(f) in the same figure), specially in the case of the p shell where distances close to 100 fm must be used in order to get convergence, as we will discuss when we study the $\sqrt{\rho}$ method. Since in all these cases it was not possible to extract reasonable values for the first overlap function, we do not show the incorrect results for the second overlap function.

Recently Gaidorov *et al.* [21] have presented results for the overlap functions of the p -shell in ^{16}O using a method similar to fit II. The procedure was applied to the correlated OBDM of [32] computed up to 11 fm, which uses the same shell model we are considering here, with similar energies and wave functions for the $1p_{1/2}$ and $1p_{3/2}$. An averaged value for the $1p$ wave function was extracted in that reference; we will explore this possibility in the shell model. In order to compute an averaged overlap function we first assume that the multipoles of the OBDM (29) can be approximated by

$$\rho_l(r_1, r_2) \simeq \sum_{nj} 2(2l + 1)\phi_{nl}(r_1)\phi_{nl}(r_2) = \sum_n \psi_{nl}(r_1)\psi_{nl}(r_2) \quad (51)$$

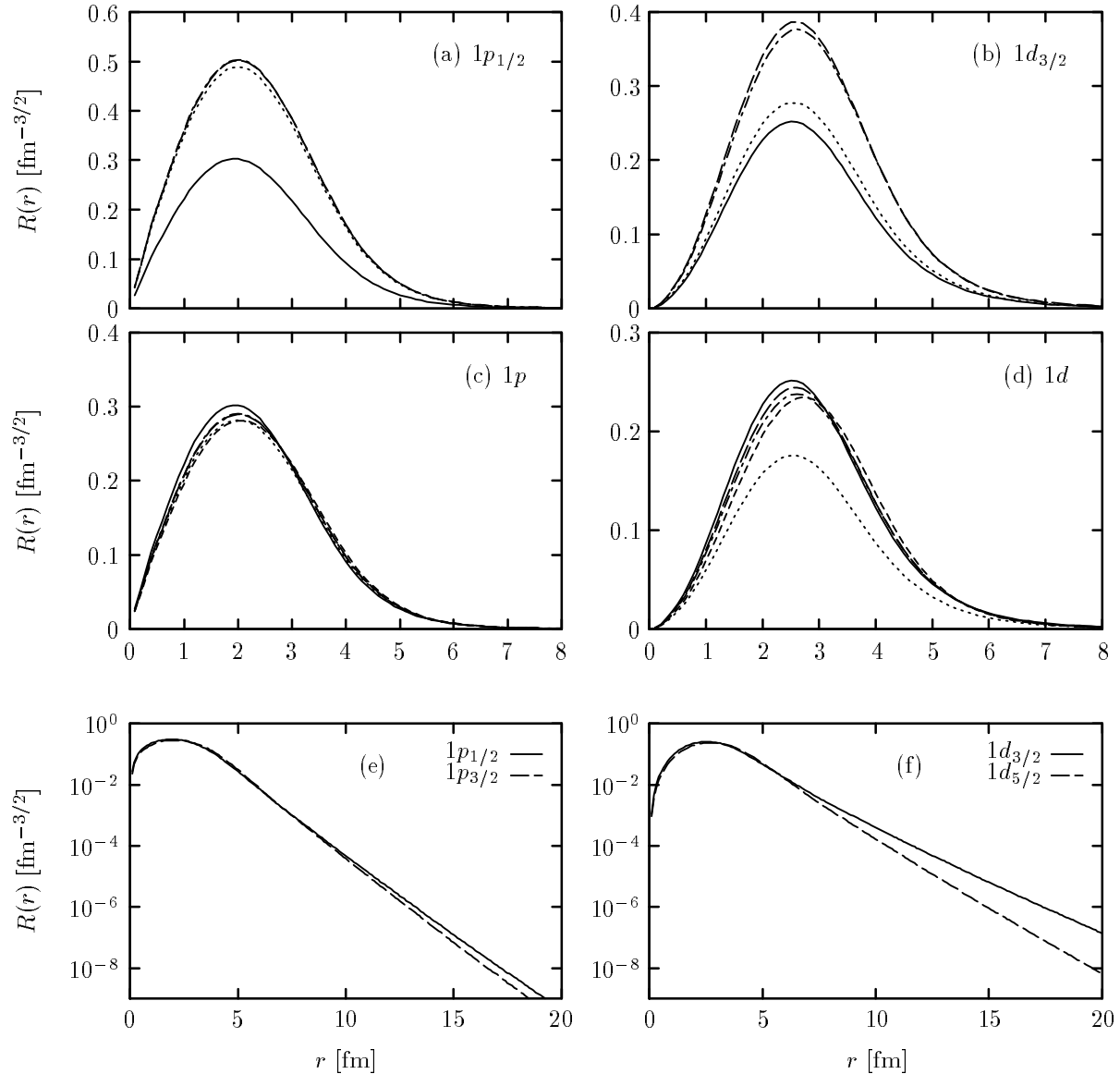


Figure 4: First overlap functions of ⁴⁰Ca for $l = 1$ and $l = 2$ in shell model, computed with the exponential decay method II. With solid lines we show the radial functions of the $1p_{1/2}$ and $1d_{3/2}$ shells, corresponding to the exact results. The asymptotic intervals $[a_l, a_u]$ considered in the fit for $l = 1$ are [4.0 fm, 11 fm] (dashed), [5.9 fm, 15 fm] (dot-dashed) and [13.0 fm, 20 fm] (dotted); for $l = 2$ they are [4.5 fm, 11 fm] (dashed), [6.6 fm, 15 fm] (dot-dashed) and [17.2 fm, 20 fm] (dotted). In panels (c) and (d) the overlap functions have been “averaged” dividing by $[2(2l + 1)]^{1/2}$ instead of $[2j + 1]^{1/2}$, and also the wave functions of the $1p_{3/2}$ and $1d_{5/2}$ shells are shown with short-dashed lines. In panels (e) and (f) the asymptotic behavior of the p and d wave functions has been displayed.

where $\phi_{nl}(r)$ is a mean value of the two spin-orbit partners $\phi_{nlj}(r)$, with $j = l \pm 1/2$. The overlap function $\psi_{nl}(r)$ is now normalized with a factor $[2(2l + 1)]^{1/2}$, and we assume an asymptotic exponential behavior $\psi_{nl}(r) \sim C \exp(-kr)/r$. Hence we have for the OBDM

$$\rho_l(r, r') \sim \psi_{nl}(r) C \frac{e^{-kr'}}{r'}, \quad r' \rightarrow \infty. \quad (52)$$

Now we can proceed as before, by fitting an exponential decay to the OBDM, and computing the averaged overlap function as $\phi_{nl}(r) = \psi_{nl}(r)/[2(2l + 1)]^{1/2}$.

Results for the averaged overlap functions of the $1p$ and $1d$ shells of ^{40}Ca obtained by this procedure are shown in panels (c)–(d) of Fig. 4. The meaning of the lines and the asymptotic intervals used in the fits are the same as in panels (a)–(b), but here we also include, for comparison, the radial wave functions of the $1p_{3/2}$ and $1d_{5/2}$ shells with short-dashed lines. Note that the overlap functions displayed in panels (c)–(d) are related to the ones of (a)–(b) just by a global factor $[(2j + 1)/2(2l + 1)]^{1/2}$.

We begin discussing the results for the $1p$ shell shown in panel (c). The fits shown with dashed and short-dashed lines are on average in the intermediate region between the $1p_{1/2}$ and $1p_{3/2}$ curves. However for higher values of the asymptotic interval (dotted lines) the fit begin to move out of this region, —it is now similar to the $1p_{3/2}$ wave function— and the possibility of obtaining an average value breaks down. The case of the $1d$ shell (d) is more intriguing. While dashed and short-dashed lines are between the $d_{3/2}$ and $d_{5/2}$ curves, the dotted lines are well below them. The conclusion extracted from these results is that only for low values of the asymptotic interval $[a_l, a_u]$ used in the fit a mean value of the overlap function is provided. However the results are unstable, since they change when another interval in the fit is used, and depend on the particular l -shell.

This behavior can be easily explained in the shell model. For example in the case of the p shell, the exact OBDM is computed as

$$\rho_1(r, r') = 2R_{1p_{1/2}}(r)R_{1p_{1/2}}(r') + 4R_{1p_{3/2}}(r)R_{1p_{3/2}}(r'). \quad (53)$$

As seen in panel (e) of Fig. 4, the wave functions of the two partners $1p_{1/2}$ and $1p_{3/2}$ are quite similar for low r . We note that they are also similar in the asymptotic region up to ~ 11 fm, since their energies are very close. So we obtain the following approximation for the OBDM up to ~ 11 fm

$$\rho_1(r, a) \simeq 6R_{1p}(r)R_{1p}(a) \quad (54)$$

and for a large, but not exceeding ~ 11 fm the two wave functions have a similar exponential behavior so we can write

$$\rho_1(r, a) \sim \sqrt{6}R_{1p}(r)C \frac{e^{-ka}}{a}, \quad a \rightarrow 11 \text{ fm} \quad (55)$$

and then it is possible to extract $R_{1p}(r)$ between the two partners, as it is shown in panel (c) with dashed lines, where $a \leq 11$ fm. For larger values of a the two wave functions

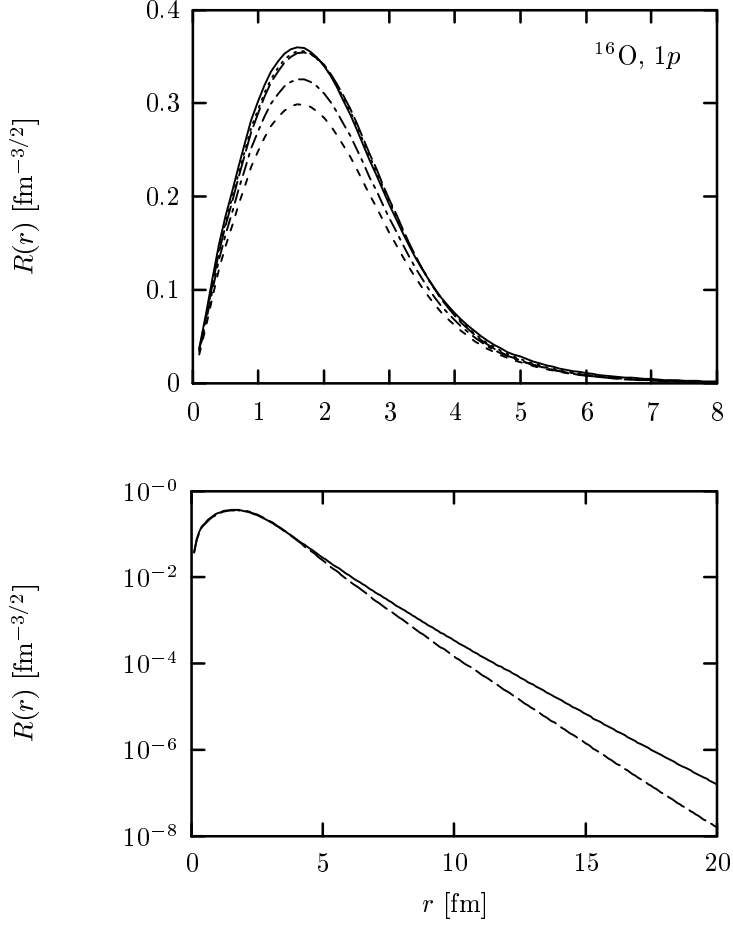


Figure 5: Averaged overlap function of the p shell of ^{16}O in shell model, computed using fit II in the asymptotic intervals [3.5,11] fm (dotted lines), [9.5,15] fm (dot-dashed lines), and [12.2, 20] fm (short-dashed lines). The exact functions of the $1p_{1/2}$ and $1p_{3/2}$ shells are shown with solid and long-dashed lines respectively.

begin to separate due to the different exponential decay. For the interval [6.6, 15] fm (dot-dashed lines in panel (c)) the two wave functions are still quite close and eq. (55) remain approximately valid. However, for the dotted lines the asymptotic interval is [13,20] fm, where the two wave functions are clearly different and eq. (55) is not valid. In this case the exact asymptotic behavior

$$\begin{aligned}
 \rho_l(r, a) &\sim 4R_{1p_{3/2}}(r)C_1\frac{e^{-k_1a}}{a} + 2R_{1p_{1/2}}(r)C_0\frac{e^{-k_0a}}{a} \\
 &\simeq R_{1p}(r)\frac{4C_1e^{-k_1a} + 2C_0e^{-k_0a}}{a}
 \end{aligned} \tag{56}$$

should be used. The exponential fit of this equation may be performed, but the result will not be the searched quantity $R_{1p}(r)$ and will depend on the interval $[a_l, a_u]$ used and

on the fitting method. In addition, in the very far limit where the second overlap can be neglected, the fit procedure will converge to the exact first overlap function $\psi_0(r) = \sqrt{2j+1}R_{1p_{1/2}}(r) = \sqrt{2}R_{1p_{1/2}}(r)$. Since the pro-mediated overlap function is computed dividing to $[2(2l+1)]^{1/2} = \sqrt{6}$, by this procedure the “averaged” overlap function will converge to the wrong result $\phi(r) = \sqrt{1/3}R_{1p_{1/2}}$.

Finally, in the $l = 2$ case, the energy difference between the $1d_{3/2}$ and $1d_{5/2}$ shells is bigger than in the case of the p -shell. This makes that the two wave functions separate at shorter distances ~ 8 fm, as seen in Fig. 4, panel (f). This implies that the results are less satisfactory than for the p -shell for high asymptotic interval (see dot-dashed lines in panel (d)). These are clear indications of the impossibility of extracting an averaged overlap function using this method.

The interesting example of the p -shell in ^{16}O is shown in Fig. 5. Therein we show with solid and dashed lines the corresponding wave functions of the $1p_{1/2}$ and $1p_{3/2}$ shells, which are very close below 5 fm, where they begin to separate. In the upper panel we also show with dotted lines the averaged overlap function obtained with fit II in the asymptotic region [3.5,11] fm, which should correspond to the mentioned calculation by Gaidorov *et al.*, in ref. [21]. The dotted line is between the two p -shell wave functions, but if the same fit is applied to higher asymptotic intervals we obtain the dot-dashed and short-dashed curves of the figure, that are below the exact result.

This example clarifies why the results of ref. [21] are not far wrong in this particular case of ^{16}O , since they used an OBDM computed up to 11 fm. However the way in which the average is done is not under control. So in the correlated case one should be careful in the interpretation of the results, because the exact ones are not known *a priori*, and the effects due to correlations cannot be unambiguously separated from the fit procedure.

4.2 $\sqrt{\rho}$ method.

Next we examine the alternative method based in eq. (37), where the overlap function is directly computed as the quotient

$$\psi_0(r) = \frac{\rho(r, a)}{\sqrt{\rho(a, a)}}, \quad (57)$$

for a value of a large enough to reach convergence, which can be easily checked by computing for several values of a . This method has several advantages over the exponential fits previously analyzed. First it has not adjustable parameters and no numerical minimization has to be carried out. Second, the OBDM has not to be calculated in an interval $[a_l, a_u]$, but only in a few asymptotic points a . This is preferable in the correlated case, where the computation of OBDM becomes longer. Moreover, when the density is factorizable $\rho(r, r') = \psi(r)\psi(r')$, then eq. (57) always provides the exact overlap function for

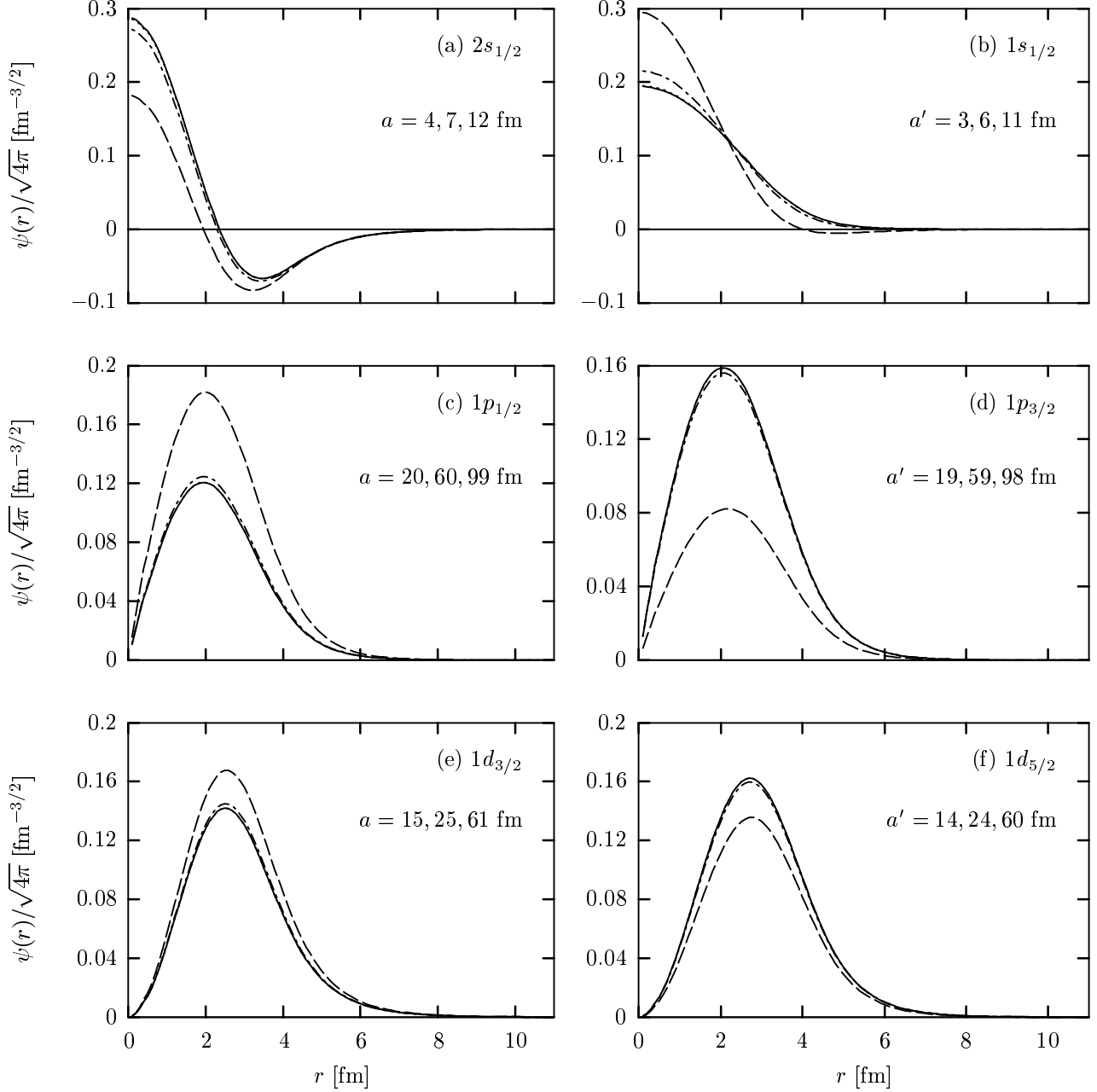


Figure 6: Overlap functions of ^{40}Ca in shell model computed with the $\sqrt{\rho}$ method. All the functions are normalized with a factor $\sqrt{(2j+1)}/4\pi$. In each panel we use the three indicated values of the asymptotic point a , that correspond in ascending order to the dashed, dot-dashed and dotted lines respectively. The exact result is shown with solid lines. The second overlap functions (panels on the right) have been computed using the first overlap function from the corresponding left panel and a second asymptotic point $a' = a - 1$ fm.

any value of a . This makes this method exact in the shell model for all the shells in ^{12}C and ^{16}O .

In Fig. 6 we show results for the non trivial case of ^{40}Ca in which two overlap functions are present for each l . In this case the asymptotic expression of the OBDM can be written

$$\rho_l(r, a) \sim \frac{e^{-k_0 a}}{a} [\psi_0(r)C_0 + \psi_0(r)C_1 e^{(k_0 - k_1)a}]. \quad (58)$$

and a should be chosen large enough in order to neglect the second overlap function. An appropriate value of a can be obtained by imposing $\exp[(k_0 - k_1)a] = 10^{-3}$. This makes the second overlap function contribution to be of the order 0.1%. The estimated value of a so obtained is

$$a \simeq \frac{6.9}{k_1 - k_0}. \quad (59)$$

However, in practice the convergence will be reached at a different value, depending on the relative value of the constants C_0 and C_1 . In the shell model we will determine the adequate value of a by comparing with the exact result.

The case of the $2s_{1/2}$ shell of ^{40}Ca is shown in panel (a) of Fig. 6. Therein we represent the first overlap function normalized with a factor $\sqrt{(2j+1)/4\pi}$, and computed from eq. (57) for three different values of a . Namely we show the results for $a = 4$ fm with dashed lines, $a = 7$ fm with dot-dashed lines, and $a = 12$ fm with dotted lines. Using this last value we already reproduce, within the scale of the figure, the exact overlap function shown with solid lines. This value is in agreement with $a \simeq 11.5$ fm provided by eq. (59).

For each one of the curves presented in panel (a) we compute the second overlap function using an asymptotic point a' that must be less than a . This is clear if we remember that the method matches the asymptotic behaviors of the OBDM and of the first overlap function for distances $r \geq a$. Then when we build the subtracted density the asymptotic contribution will vanish in this region. This is equivalent to say that the point a effectively acts as the infinite point $a \simeq \infty$, so in this numerical method it has no sense to compute the second overlap function for $a' > a$. For this reason, the second overlap functions for $l = 0$ displayed in panel (b) of Fig. 6, have been computed for asymptotic point $a' = a - 1$ fm. Again for the biggest value shown, the extracted overlap function almost coincides with the exact result shown with solid lines.

Results for the remaining shells $l = 1, 2$ are shown in panels (c)–(f). As before, we show in each panel three curves corresponding to three ascending values of a indicated in the figure, with dashed, dot-dashed and dotted lines respectively. In the case of the second overlap function (panels on the right) we use the corresponding first overlap function of the left panel and asymptotic point $a' = a - 1$ fm. The values of a for which convergence of the first overlap function is obtained are shown in table 3. In the case of the p -shell (panels (c) and (d)), we find convergence for $a \sim 100$ fm. Using the single-particle energies of table 2 and eq.(59), we obtain $a \simeq 86$ fm for the p - shell and $a \simeq 60$ for the d -shell.

Nucleus	$2s_{1/2}$	$1p_{1/2}$	$1d_{3/2}$
^{16}O		80	
^{40}Ca	12	100	61
^{48}Ca	12	> 100	98

Table 3: Values of the asymptotic points for which convergence of the first overlap function is reached with the $\sqrt{\rho}$ method.

We have performed the same study of the proton overlap functions using the $\sqrt{\rho}$ method for other closed-shell nuclei. The results of the convergence values for ^{16}O and ^{48}Ca are summarized in table 3. In the case of ^{16}O we only show the non-trivial case of the p -shell. The corresponding overlap functions can be separated by using the OBDM computed up to $a \simeq 80$ fm. Finally, In the case of ^{48}Ca , the separation energy within the p - and d -shells is smaller than in ^{40}Ca (see table 2). As a consequence, the convergence values are larger than in the former case. In particular, for $a = 100$ fm the $1p_{1/2}$ and $1p_{3/2}$ are not completely separated and the convergence value is not shown in the table. The estimated value of convergence for this shell is $a = 138$ fm.

As a summary of this section, with our present study using the shell model, we have shown the reliability of the asymptotic methods to compute the overlap functions of nuclei from the knowledge of the l -multipoles of the OBDM. Our results have shown the necessity of studying the convergence of the results in each case and that in many of them one should calculate the OBDM up to such huge distances as 100 fm in order to separate the overlap functions. In relation to the several methods studied, all of them provide the correct result if the asymptotic interval $[a_l, a_u]$ is within the region of convergence. However, due to its simplicity, the $\sqrt{\rho}$ method is preferable in the general case in which the OBDM is the solution of a correlated many-body problem, and this is the method we will use in the next section to compute the correlated overlap functions.

5 Results for $(e, e'p)$ observables and overlap functions in the correlated case

In this section we present results for overlap functions, spectroscopic factors, $(e, e'p)$ response functions, and cross sections, using the correlated model introduced in section 3. Thus we go beyond the single-particle model and will be able to identify the effects of short-range correlations on these quantities and observables.

5.1 Quasi-hole overlap functions

We start with the correlated OBDM of closed-shell nuclei, defined by eq. (43), and compute the multipoles, $\rho_l(r, r')$, as shown in ref. [22]. The zero-order density $\rho_l^0(r, r')$ in eq. (43) corresponds to the non correlated shell model of sect. 4. The correlated overlap functions for quasi-hole states can be obtained by using the $\sqrt{\rho}$ method discussed in the last section. We apply eq. (57) to the correlated OBDM for asymptotic points, a , large enough to reach convergence. In the present case the exact result are not known *a priori*, but we are guided by the former study performed in the shell model. It is expected that the values of the convergence asymptotic points in the correlated case do not change too much respect to the shell model ones. This can be understood in our model by studying the correlated OBDM, eq. (43). Using the fact that the correlation function $f(r) \rightarrow 1$ for $r \rightarrow \infty$, we have for the function H defined in (44)

$$H(\mathbf{r}_1, \mathbf{r}'_1, \mathbf{r}_2) \sim Q(1)[f(r_{12}) - 1], \quad r'_1 \rightarrow \infty. \quad (60)$$

On the other hand, the non-correlated density is dominated asymptotically by the first overlap function of the shell model

$$\rho_0(\mathbf{r}_1, \mathbf{r}'_1) \sim \phi_0(\mathbf{r}_1)\phi_0(\mathbf{r}'_1) \quad r'_1 \rightarrow \infty. \quad (61)$$

From these equations it is straightforward to obtain the following asymptotic expression for the correlated density (43) for $r'_1 \rightarrow \infty$

$$\rho_1^p(\mathbf{r}_1, \mathbf{r}'_1) \sim K(\mathbf{r}_1)\phi_0(\mathbf{r}'_1) \quad r'_1 \rightarrow \infty \quad (62)$$

where the function $K(\mathbf{r}_1)$ is defined as

$$\begin{aligned} K(\mathbf{r}_1) \equiv & \phi_0(\mathbf{r}_1) + \phi_0(\mathbf{r}_1) \int d^3r_2 Q(1)[f(r_{12}) - 1] \rho_0(\mathbf{r}_2, \mathbf{r}_2) \\ & - \int d^3r_2 \rho_0(\mathbf{r}_1, \mathbf{r}_2) Q(1)[f(r_{12}) - 1] \phi_0(\mathbf{r}_2) \\ & - \int d^3r_2 \int d^3r_3 \rho_0(\mathbf{r}_1, \mathbf{r}_2) \phi_0(\mathbf{r}_2) \rho_0(\mathbf{r}_3, \mathbf{r}_3) H(\mathbf{r}_2, \mathbf{r}_2, \mathbf{r}_3) \\ & + \int d^3r_2 \int d^3r_3 \rho_0(\mathbf{r}_1, \mathbf{r}_2) \rho_0(\mathbf{r}_2, \mathbf{r}_3) \phi_0(\mathbf{r}_3) H(\mathbf{r}_2, \mathbf{r}_2, \mathbf{r}_3) \end{aligned} \quad (63)$$

We can also determine the asymptotic behavior of this function $K(\mathbf{r}_1)$ by using the particular Gaussian form (41) of the correlation function, so for $r_1 \rightarrow \infty$ the second and third terms in (63) can be neglected with respect to the other terms due to its Gaussian decay. Then we can write

$$K(\mathbf{r}_1) \sim \eta \phi_0(\mathbf{r}_1), \quad r_1 \rightarrow \infty \quad (64)$$

where the constant η is defined as

$$\begin{aligned} \eta \equiv & 1 - \int d^3r_2 \int d^3r_3 |\phi_0(\mathbf{r}_2)|^2 \rho_0(\mathbf{r}_3, \mathbf{r}_3) H(\mathbf{r}_2, \mathbf{r}_2, \mathbf{r}_3) \\ & + \int d^3r_2 \int d^3r_3 \phi_0(\mathbf{r}_2) \rho_0(\mathbf{r}_2, \mathbf{r}_3) \phi_0(\mathbf{r}_3) H(\mathbf{r}_2, \mathbf{r}_2, \mathbf{r}_3). \end{aligned} \quad (65)$$

Using now the $\sqrt{\rho}$ method, the first correlated overlap function reads

$$\psi_0(\mathbf{r}) = \lim_{r' \rightarrow \infty} \frac{K(\mathbf{r})\phi_0(\mathbf{r}')}{\sqrt{K(\mathbf{r}')\phi_0(\mathbf{r}')}} = \frac{K(\mathbf{r})}{\sqrt{\eta}}. \quad (66)$$

Since the function $K(\mathbf{r}) \sim \eta\phi_0(\mathbf{r})$, for $\mathbf{r} \rightarrow \infty$, we see that this correlated overlap function behaves asymptotically as the non-correlated one multiplied by the constant $\sqrt{\eta}$

$$\psi_0(\mathbf{r}) \sim \sqrt{\eta}\phi_0(\mathbf{r}), \quad r \rightarrow \infty \quad (67)$$

Hence in the present model the short-range correlations do not modify the energy of the first overlap function respect to the shell model, since the asymptotic behavior of the OBDM is determined by the exponential decay of the single-particle wave function $\phi_0(\mathbf{r})$. Note that for shorter distances the above proportionality (67) does not hold because, in that case, the function $K(\mathbf{r})$ includes other terms depending on the non correlated density and on the correlation function $f(r)$, as can be seen in eq. (63).

The same procedure can be applied to each one of the multipoles $\rho_l(r, r')$ to show that the energy of the first overlap function for each value of l does not change respect to the uncorrelated case. The same conclusion was also obtained in ref. [15] in a model similar to ours by starting with the OBDM $\rho_{lj}(r, r')$. However in our model it is not possible to prove easily a similar result for the energy of the *second* overlap function.

These arguments indicate that the asymptotic points needed to compute the overlap functions are similar to the ones found in the shell model. In any case, in our calculations we have checked numerically the convergence of the results for the different overlap functions. For this reason, the correlated OBDM has been computed for values of the asymptotic point as high as 100 fm in order to separate the first overlap function in the cases in which the energies of two overlap functions are close in the shell model. The values of the asymptotic point a where convergence is reached are given in the third column of table 4. We first note that the convergence values of the asymptotic point a are similar to the ones obtained in the shell model (compare with table 3). Thereby, in order to extract the $1p_{1/2}$ overlap function, we need to go up to ~ 86 fm for ^{16}O and up to ~ 100 fm for ^{40}Ca , while in the case of the $1d_{3/2}$ overlap function for ^{40}Ca , convergence is found for $a \sim 64$ fm. This indicates that in fact the separation energies of correlated overlap functions are close to the ones of the shell model.

The results for the correlated overlap functions of the nuclei ^{12}C , ^{16}O and ^{40}Ca are shown in figs. 7–9 respectively. In each one of these figures we show with solid lines the radial density $r^2\psi(r)^2$ of the correlated overlap function and with dashed lines the non-correlated result corresponding to the shell model. We do not show the overlap functions of the also studied nucleus ^{48}Ca . Having stopped our calculation at 100 fm, it was not possible to obtain convergence in this nucleus for the overlap function of the p -shell, which requires higher values of a .

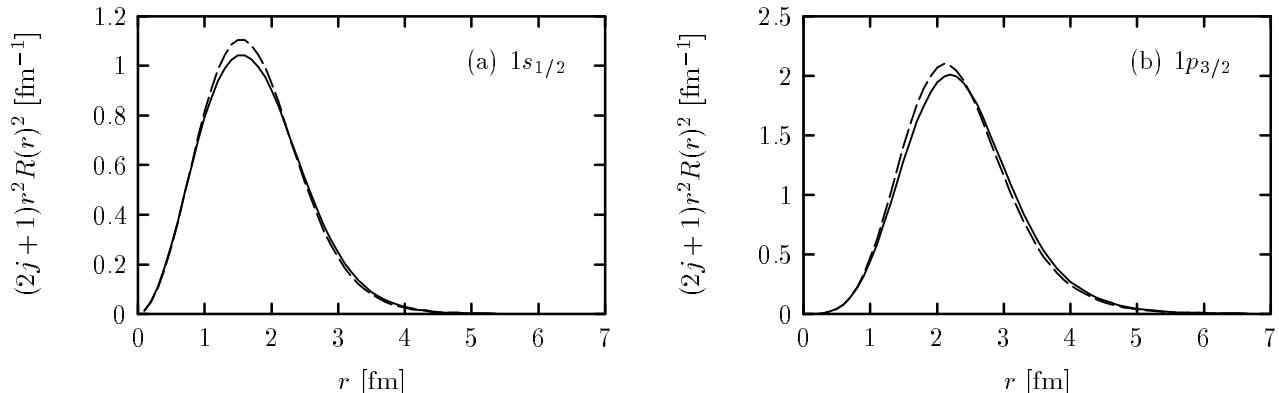


Figure 7: Solid lines: radial density of overlap functions for ^{12}C computed from the correlated OBDM. With dashed lines we show the non-correlated results in the shell model.

In figure 7 we show the first overlap functions of ^{12}C for $l = 0, 1$. In both cases convergence is reached for relatively small values of $a = 7$ and 8 fm, respectively, due to the fact that in the shell model there are no second overlap functions contributing to the OBDM. Short range correlations introduce extra contributions in the OBDM. However, these extra contributions decay much faster than the exponential one, and very large distances are not needed to extract the first overlap function. As we can see in figure 7, the inclusion of short-range correlations produces in both cases a reduction of the maximum of the overlap function in coordinate space, while there is an increase for high r , which is better seen in the case of the p -shell, since it lies at higher distances (panel (b)). In this last case we observe in addition that the overlap function undergoes a small shift to the right due to the correlations.

Similar effects are observed in figs. 8 for ^{16}O and fig. 9 for ^{40}Ca . In all cases there is a reduction of the overlap function at intermediate distances (in most of them coinciding with the maximum of the radial density) and an increase for more large distances. As in ^{12}C , we also observe a shift to the right of the overlap functions corresponding to the outer shells. This is the case of the shells $1p_{1/2}$ and $1p_{3/2}$ in ^{16}O and $2s_{1/2}$, $1d_{3/2}$ and $1d_{5/2}$ in ^{40}Ca .

This shift effect over the outer shells can be understood in terms of the repulsive nature of the NN interaction for short distances, implicit in the correlation function $f(r)$, and the well known healing property of the wave function for the two-nucleon system. The correlation function produces a wound in the NN wave function Ψ , and what we are seeing in the overlap function is the average effect of healing due to the interaction of the outer nucleons with the nucleons in the core.

However the inner shells do not show this effect because the short-range repulsion due to the core partially cancels the one produced by the external shells. The net effect depends on the particular nucleus and on the shell involved. For instance, in the case of

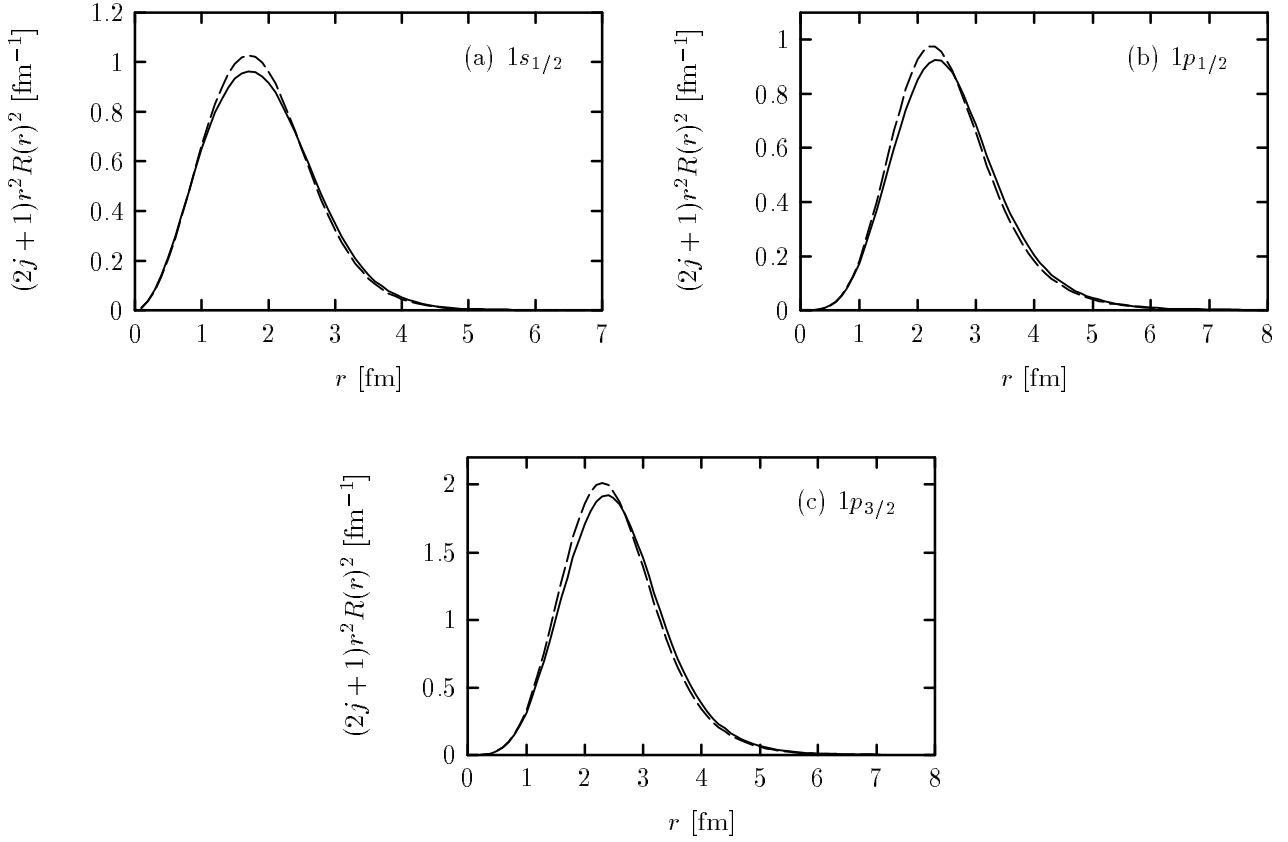


Figure 8: The same as fig. 7 for the nucleus ^{16}O .

the $1s_{1/2}$ shell in ^{40}Ca , shown in panel (b) of fig. 9, the correlations produce a shift of the overlap function to the left, i.e., into the nucleus, since the short-range repulsion by the outer shells tends to compress the $1s$ wave. The same compression effect is observed in the inner lobe of the $2s_{1/2}$ (see panel (a) of fig. 9).

In the cases of the intermediate shells $1p_{1/2}$ and $1p_{3/2}$ for ^{40}Ca the joint effect of repulsion by the inner and outer shells produces a shift to the left in the low r region and a shift to the right for large r . Hence the net effect of correlations over these shells is a widening of the overlap function, as seen in panels (c) and (d) of fig. 9.

Once the overlap functions have been extracted, we can compute the corresponding separation energy by a fit to a function $Ce^{-kr-\eta \ln kr}/r$ for large distances. We have performed this fit in the interval between 11 and 28 fm for the correlated and uncorrelated overlap functions obtaining essentially the same energies. The inclusion of the logarithm Coulomb phase is important in this fit for protons, since it can modify the extracted energies in more than 2 MeV in the case of ^{40}Ca . The relative difference between correlated and uncorrelated energies is shown in the fourth column of table 4. In all cases the differences are less than 0.5 % even in the case of the ^{48}Ca shells where convergence was

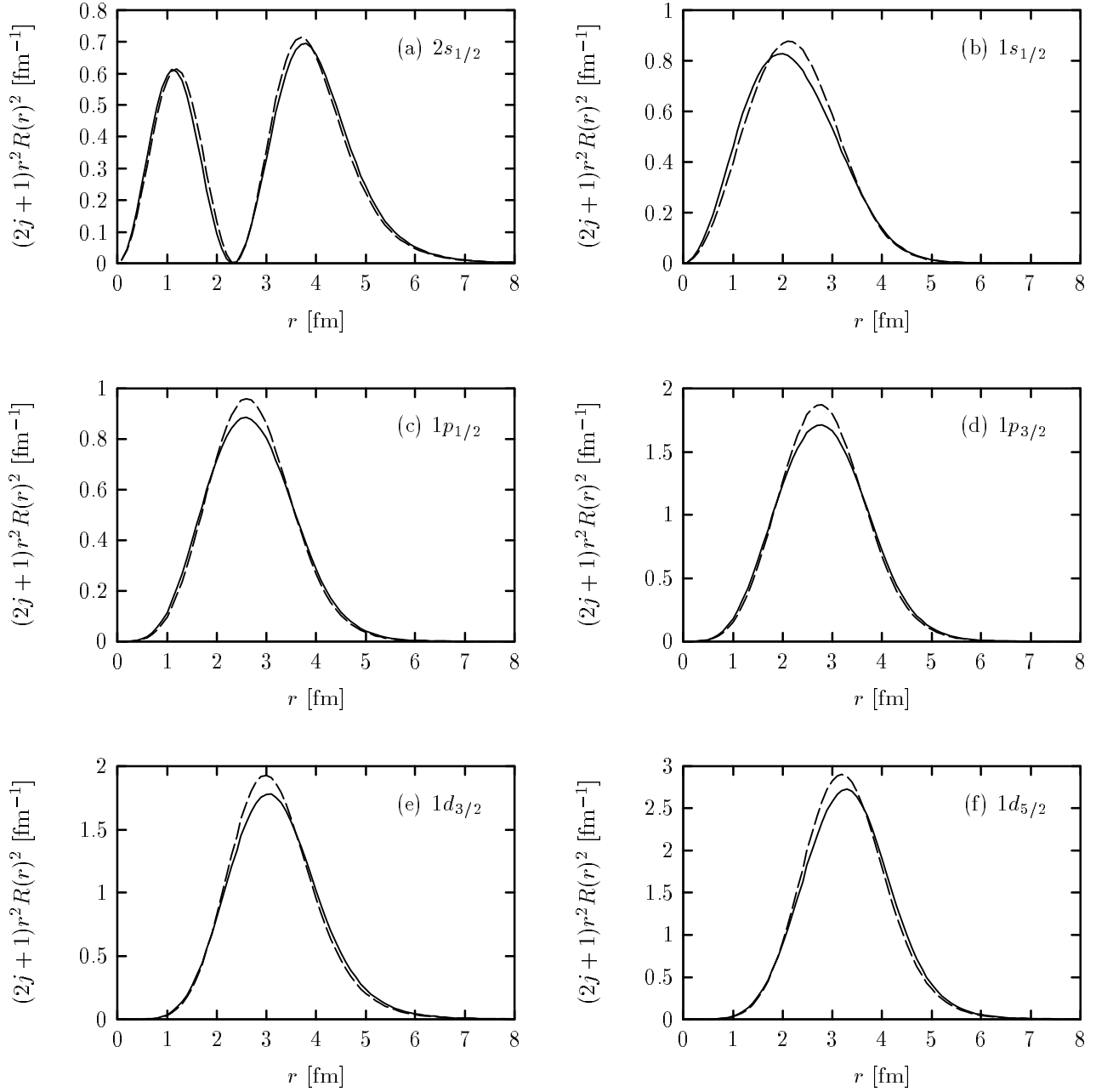


Figure 9: The same as fig. 7 for the nucleus ^{40}Ca .

Nucleus	nlj	a [fm]	$ E_c - E_{ws} /E_{ws}$ [%]	S_{th}	S_{exp}
^{12}C	$1s_{1/2}$	7	4×10^{-5}	0.985	0.59
	$1p_{3/2}$	8	$< 10^{-6}$	0.986	0.56
^{16}O	$1s_{1/2}$	7	2×10^{-5}	0.985	
	$1p_{3/2}$		7×10^{-4}	0.986	0.59
	$1p_{1/2}$	86	4×10^{-5}	0.986	0.57
^{40}Ca	$1s_{1/2}$		6×10^{-2}	0.988	0.75
	$2s_{1/2}$	14	2×10^{-3}	0.992	0.64
	$1p_{3/2}$		3×10^{-2}	0.985	0.72
	$1p_{1/2}$	100	3×10^{-3}	0.985	0.72
	$1d_{5/2}$		2×10^{-3}	0.985	0.74
	$1d_{3/2}$	64	3×10^{-5}	0.985	0.74
^{48}Ca	$1s_{1/2}$		6×10^{-4}	0.986	
	$2s_{1/2}$	16	1×10^{-1}	0.991	
	$1p_{3/2}$		2×10^{-1}	0.946	
	$1p_{1/2}$	> 100	3×10^{-1}	1.058	
	$1d_{5/2}$		1×10^{-3}	0.983	
	$1d_{3/2}$	100	6×10^{-4}	0.983	

Table 4: For each one of the quasi-hole states in the closed shell nuclei studied we show: the asymptotic distance a for which convergence of the correlated overlap function is reached (third column), the relative difference between correlated and uncorrelated separation energies (fourth column), and the computed spectroscopic factor (fifth column). For comparison we show also the experimental value of the spectroscopic factors extracted from $(e, e'p)$ experiments.

still not found for the overlap function. These numerical results confirm that short-range correlations do not change the mean field values of the separation energies for quasi-hole states.

Results for the spectroscopic factors resulting from our model are shown in the fifth column of table 4. These have been computed as the norm of the corresponding correlated overlap function

$$S = \langle \phi | \phi \rangle. \quad (68)$$

As seen in table 4, all of the computed spectroscopic factors are slightly less than one, being in most of the cases around $S \sim 0.985$. The only exception found in table 4 is the value $S_{p_{1/2}} = 1.058$ for ^{48}Ca , which is not a definitive number since the asymptotic point $a = 100$ fm used is not large enough to reach convergence in this case.

Our results indicate that short-range correlations of Jastrow-type reduce the shell model occupation probability no more than 2%. This reduction is not enough to explain the experimental values extracted from $(e, e'p)$ analysis shown in column 5 of table 4. This is in agreement with other studies which report values similar to ours for the spectroscopic

factors. Van Neck *et al.* found in [15] that central correlations generate a reduction around 1–2% of the occupancy probability in ^{16}O . More recently Fabrocini and Co' [33] have computed overlap functions within the FHNC/SOC theory and report values around 0.97–0.99 for the spectroscopic factors with Jastrow correlations. Spin-isospin and tensor correlations (not included in our calculation) produce additional reduction of these values to $S \sim 0.86$ –0.9 for the valence shells. The discrepancy with experimental values could be further reduced by the inclusion of long-range correlations [14]. Center of mass corrections however produce an enhancement of $\sim 7\%$ of the p -shell in ^{16}O [9]. Further investigation including all of these effects in a consistent way is needed in order to clarify the situation.

5.2 Quasi-particles and the continuum

Up to now we have restricted our study to overlap functions corresponding to quasi-hole states. Our correlated OBDM model allows us to compute also the multipoles $\rho_l(r, r')$ for high values of l , which are expected to contain contributions coming from quasi-particle states, i.e., states non occupied in the shell model but which are partially populated in the ground state due to nuclear correlations. We have investigated if the overlap functions for quasi-particles can be extracted from our OBDM using the asymptotic method.

This study is motivated by a recent calculation done in [19] where results for the quasi-particle overlap function for the $1d$ -shell in ^{16}O and for the $1f$ shell in ^{40}Ca are presented. These authors begin with an OBDM including Jastrow correlations and apply an asymptotic procedure similar to fit II in order to extract the overlap functions. For instance they report a value of $S = 0.01$ for the spectroscopic factor of the $1f$ shell in ^{40}Ca . Neither the asymptotic interval used for the fit nor the convergence distance are indicated in [19]. Apparently they should not have used very high asymptotic values since they use a harmonic oscillator basis that fall off rapidly at large distances.

However these results were criticized in ref. [15], where it was shown that it is not possible, starting from a CBF-type wave function, to generate bound-state overlap functions with quantum numbers that are unoccupied in the Slater determinant. The reason is that the overlap functions decay exponentially with the same decay constant as the hole single-particle orbital

In fact, when we apply the $\sqrt{\rho}$ method to compute a quasi-particle overlap function from our radial OBDM for high values of l we do not obtain convergence within the 100 fm range and instead the results decrease rapidly, being negligible for high r . We must conclude that in our model it is not possible to obtain such quasi-particle states.

This result can be understood by examining the following asymptotic expression of the OBDM for unoccupied multipole l

$$\rho_l(r_1, r'_1) \sim C f(r_1, r'_1), \quad r_1, r'_1 \rightarrow \infty \quad (69)$$

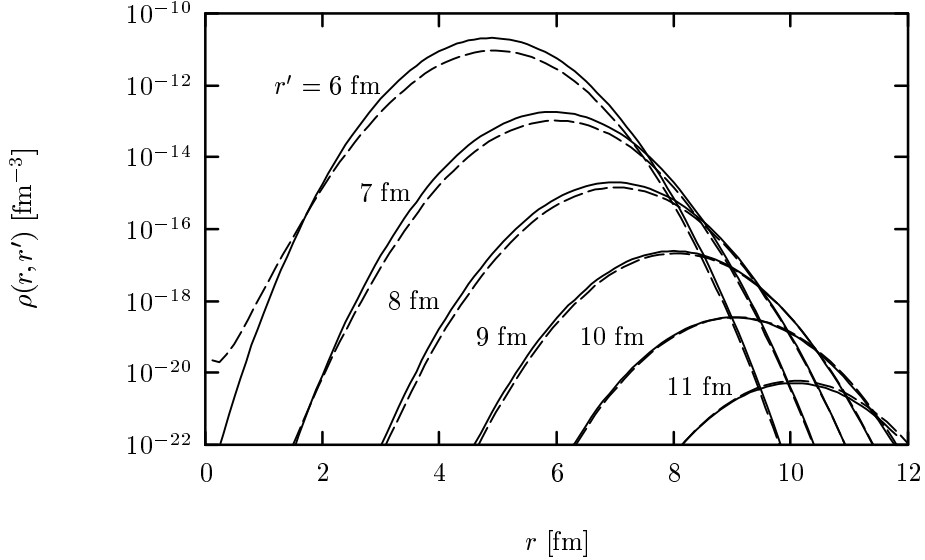


Figure 10: The solid lines are the correlated OBDM, $\rho_2(r, r')$ for $l = 2$ in ^{12}C , as a function of r for different values of $r' = 6, 7, 8, 9, 10$ y 11 fm. The dashed lines are a fit to an asymptotic approximation $f(r, r')$ defined in (70).

where C is a constant and the function $f(r, r')$ is given by

$$f(r_1, r'_1) = \frac{\exp(-2kr_1) \exp(-2kr'_1) \exp\left(\frac{-B(r_1 - r'_1)^2}{2}\right)}{r_1^2 r_1'^2 (r_1 + r'_1)^2}. \quad (70)$$

Here k is the wave number of the (occupied) valence shell and B is the parameter of the correlation function. This expression is proved in Appendix B for the simplest case of the multipole $l = 2$ for the nucleus ^{12}C .

In figure 10 we show with solid lines the computed radial density $\rho_2(r, r')$ for ^{12}C as a function of r for several fixed values of r' . In addition we show with dashed lines the function $f(r, r')$ multiplied by a convenient constant C fitted to the density. We see that in fact the above asymptotic expression is approximately verified by the computed density for high values of r and r' .

If we now try to compute a quasi-particle overlap function using the $\sqrt{\rho}$ method we obtain

$$\psi_l(r) = \frac{\rho_l(r, a)}{\sqrt{\rho_l(a, a)}} \sim \frac{2a}{r^2 (r + a)^2} \rho_0(r) e^{-B(r-a)^2/2} \quad (71)$$

this expression goes to zero for $a \rightarrow \infty$, since the diagonal part of ρ_l has an exponential decay, while the non-diagonal part has an additional Gaussian behavior corresponding to the correlation function. This explains why in our results the extracted overlap function for quasi-particles are zero. Thus in our model of correlated OBDM it is not possible

to obtain the overlap functions for quasi-particles since the corresponding information of single-particle states above the Fermi level (configuration mixing) has not been included into the model. Moreover, when one subtract from the correlated OBDM the contribution of the quasi-hole states the remaining density contains only the contributions coming from the *continuum* states of the residual nucleus. These contributions are implicit in the expansion (27) in terms of overlap functions and they can be expressed as an integral over the energy.

$$\rho(\mathbf{r}, \mathbf{r}') - \rho_{quasi-hole}(\mathbf{r}, \mathbf{r}') = \int dE \Psi_E(\mathbf{r})^\dagger \Psi_E(\mathbf{r}') \quad (72)$$

With the asymptotic method studied here it is not possible to extract these overlap functions of the continuum. For this a practical inversion method of the integral (72) in the asymptotic region is needed. The knowledge of these overlap functions would be of interest, for instance, to compute the $(e, e'p)$ cross section for high missing energy.

5.3 Exclusive response functions and cross sections

In figs. 11–13 we show the five exclusive responses for proton knockout from the valence shells of the nuclei ^{12}C , ^{16}O and ^{40}Ca , as a function of the missing momentum. In all the cases the kinematics correspond to a fixed value of the momentum transfer $q = 460$ MeV/c and ω fixed around the quasi-elastic peak. In each panel of figs. 11–13 we show four curves corresponding to different models for the initial and/or final wave functions that enter in the current matrix element (7). We show results for PWIA and DWIA with and without short-range correlations in the initial state overlap functions. The DWIA results have been obtained using for the FSI the optical potential of ref. [35]. Specifically, the solid lines have been computed with the DWIA model and using correlated overlap functions, while the dashed lines do not include correlations. Thus comparison between solid and dashed lines shows the effect of short-range correlations in the responses. Results in PWIA with and without correlations are shown with short-dashed and dotted lines, respectively.

In all the cases we note in the region $p < 200$ MeV/c an increase of the L, T and TL responses due to correlations, which is around 5% near the maximum. This increase is quite independent on the FSI since it is also present in PWIA. The reason for this fact is that correlations between the ejected proton and the residual nucleus have not been included. The increase seen in the responses can be easily understood in PWIA, where we are basically seen the momentum distribution of the shell, as a consequence of the hardening effect seen in the overlap functions in figs. 7–9 for the valence shells. Since in momentum space the low p region is sensitive to the high r region, the increase of the overlap function for high r translates into an increase of the Fourier transform for low p (~ 100 MeV/c) where the maximum of the momentum distribution is located. Since the correlations in the ground state are in some degree decoupled from the FSI, the same effect is propagated to the case of the DWIA.

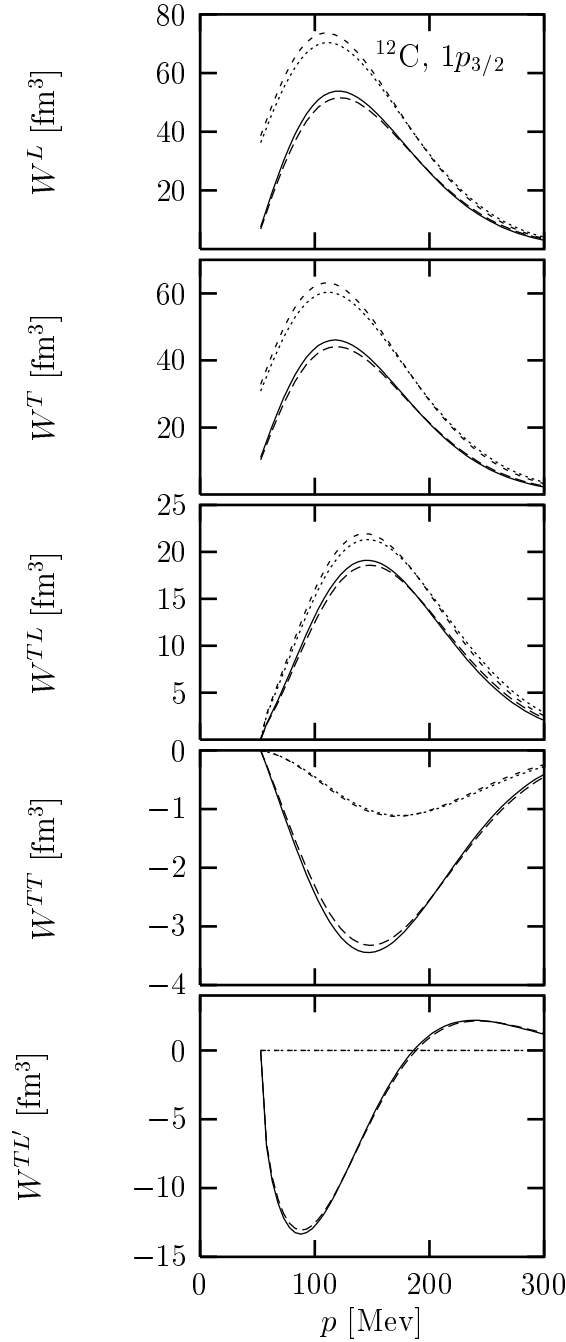


Figure 11: Response functions for proton knock-out from the $p_{3/2}$ shell in ^{12}C , for $q = 460$ MeV and ω at the quasi-elastic peak. Results are shown in DWIA with (solid lines) and without (dashed lines) correlations in the hole overlap function, and in PWIA with (short-dashed lines) and without (dotted lines) correlations.

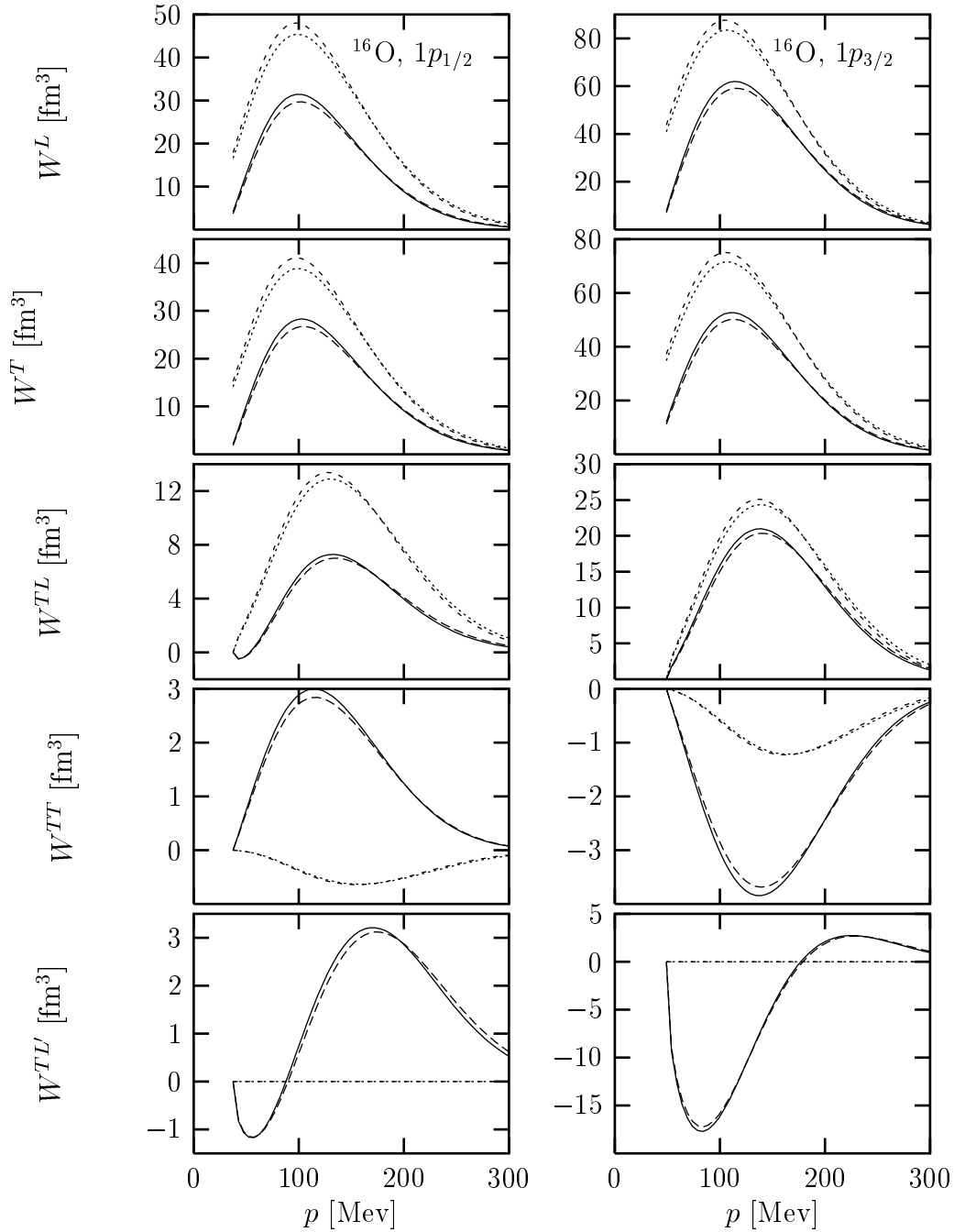


Figure 12: Response functions for proton knock-out from the valence shells, $1p_{3/2}$ and $1p_{1/2}$, in ^{16}O , for $q = 460$ MeV and ω at the quasi-elastic peak. The meaning of the lines is the same as in fig. 11.

In the case of the TT response, we also find an increase of its absolute value due to correlations in DWIA, which is not seen in PWIA because the leading-order magnetization current do not contribute to this response [23], and the resulting factorized single-nucleon TT response is of order $(p/M)^2$ in a non-relativistic expansion (this is the reason why this response function is so small). This kinematical dependence comes exclusively from the convection current, producing a hardening of the maximum of the momentum distribution toward higher p -values ~ 150 MeV, where the correlated and uncorrelated results are closer. In DWIA, the FSI breaks the factorization property and the magnetization current gives a contribution which wherefore is much larger than the PWIA result.

Regarding the fifth response function TL' , which only can be measured using polarized electrons, it is exactly zero in absence of FSI. In DWIA however it produces a contribution to the total cross section and the correlations in the ground state produce an increase which is in general of the same order as in the unpolarized responses. This increase is even more large ($\sim 15\%$) in the case of the $1d_{3/2}$ shell in ^{40}Ca (see fig. 13).

State-independent short-range correlations produce an increase of the $(e, e'p)$ cross section, since the later is a linear combination of the several response functions appearing in eq. (1). An example is shown in fig. 14, where results of DWIA calculations for the reaction $^{16}\text{O}(e, e'p)$ are displayed together with the experimental data of ref. [36]. Here the kinematics correspond to fixed momentum transfer $q = 570$ MeV/c and energy transfer $\omega = 170$ MeV, at the quasi-elastic peak. The energy of the electron beam is 580 MeV and the proton is emitted in the scattering plane. In fig. 14 we show with solid lines our DWIA results using the correlated overlap functions for the $1p_{1/2}$ and $1p_{3/2}$ shells, while with dashed lines we show the uncorrelated results. We note an enhancement of the cross section due to correlations which is of the same order of magnitude as was found for the response functions, and which clearly increases the disagreement between theory and experiment. In the same figure we show with short dashed and dotted lines the computed cross sections multiplied by the factors 0.6 ($1p_{1/2}$) and 0.5 ($1p_{3/2}$) in the correlated case and 0.64 ($1p_{1/2}$) and 0.53 ($1p_{3/2}$) in the uncorrelated one.

Hence the scaling factor needed to reproduce the experimental cross section is *smaller* for correlated than for uncorrelated overlap functions even though the computed spectroscopic factors for these shells are smaller than one, $S = 0.985$ (see table 4). This fact does not necessarily imply a decrease of the *experimental* spectroscopic factors since these are obtained by a simultaneous fit of the parameters of the single particle potential also. In other words, experimentally one searches for the best phenomenological overlap function that when included into an uncorrelated DWIA code reproduces the experimental data. Our model has not adjustable parameters since the correlations are already included and so are the spectroscopic factors. Our results are showing that short-range correlations of the central-type in the ground state do not produce an improvement of the $(e, e'p)$ data description. Tensor correlations and long-range correlations are obvious candidates for a reconciliation between theory and experiment.

To end the discussion we give in fig. 15 another application of our DWIA model in photo-nuclear reactions. Therein we show the computed (γ, p) cross section from the

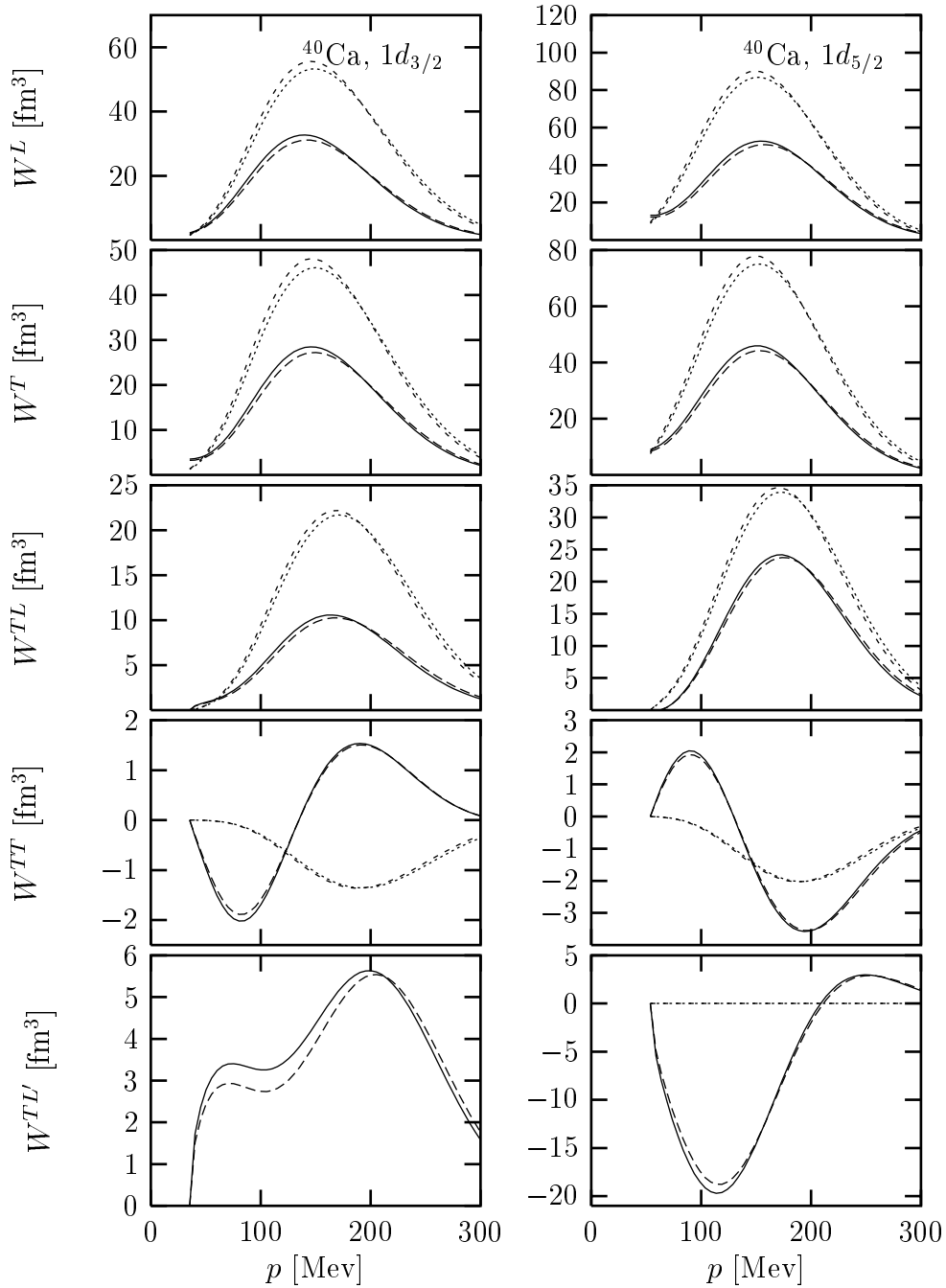


Figure 13: Response functions for proton knock-out from the valence shells, $1d_{5/2}$ and $1d_{3/2}$, in ^{40}Ca , for $q = 460$ MeV and ω at the quasi-elastic peak. The meaning of the lines is the same as in fig. 11.

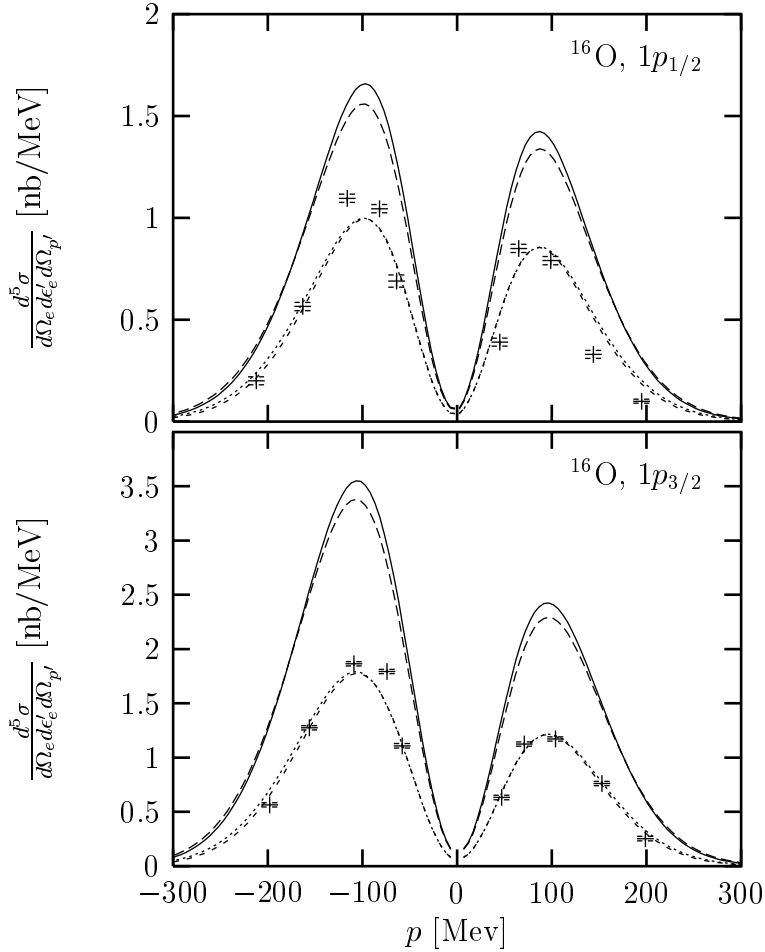


Figure 14: Computed $(e, e'p)$ cross section for the valence shells of ^{16}O . The solid lines include correlated overlap functions while the dashed lines do not. These calculations have been scaled to give the dashed and dotted lines in order to reproduce the experimental data from ref. [36].

$1p_{1/2}$ shell in ^{16}O for two beam energies of $E_\gamma = 60$ and 72 MeV together with the experimental data of ref. [37]. Again we show with solid and dashed lines the correlated and uncorrelated results respectively. No scaling factors are included. The impact of central correlations in this case is completely different from the $(e, e'p)$ reaction. In this case they produce a large reduction of the cross section. The difference between the two reactions lies in the different kinematical region which is being probed by photons. In the case of (γ, p) the energy-momentum transfer verifies $\omega = q$ and we are far from the quasi-elastic peak region. As a consequence the missing momentum is well above 200 MeV/c. Thus apart from the small values of q , the photon is exploring here the high momentum tail of the overlap function where correlations produce a reduction of the momentum distribution. Such reduction can also be appreciated in figs. 11–13, where the correlated transverse response (the one contributing to photo-reactions) is below the uncorrelated

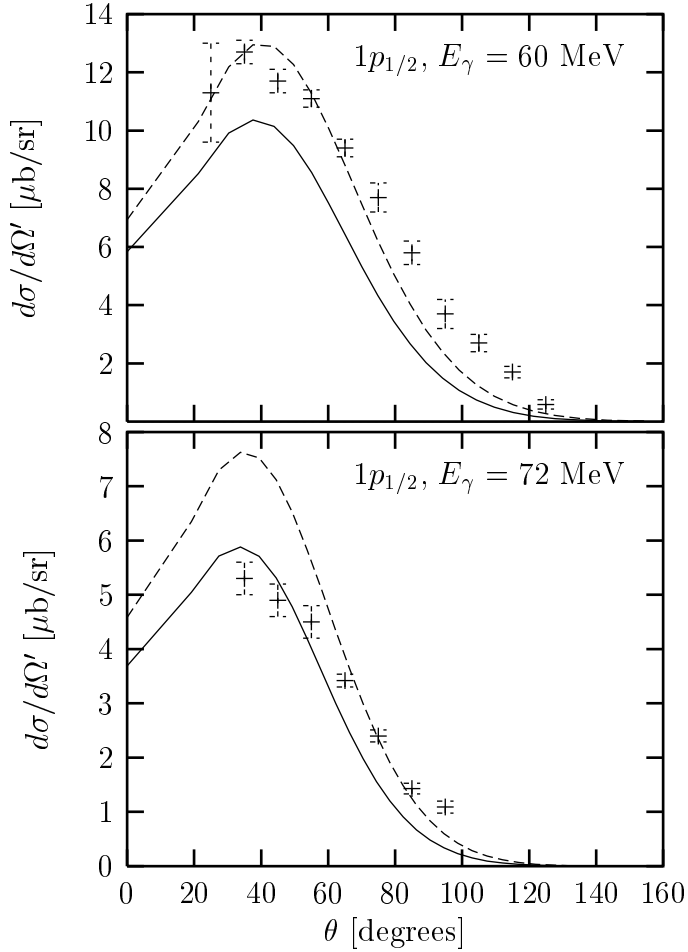


Figure 15: Computed (γ, p) cross section for the $1p_{1/2}$ shell of ^{16}O . The solid lines include correlated overlap functions while the dashed lines do not. Experimental data are from ref. [37]

one for $p > 200$ MeV/c. One should also be aware of the difficulties presents in the DWIA description of the (γ, p) reaction for so low energies and high missing momenta, where in particular the orthogonality approximation (10) is no longer true and other effects [38] of the same order as the ones arising from correlations could appreciably change the results of fig. 15.

6 Summary and Conclusions

In this work the effects of short-range correlations on $(e, e'p)$ observables and overlap functions have been studied. The starting point for the present calculation has been the OBDM, including short-range correlations of central Jastrow type, and which has been computed by a cluster expansion to leading order in the correlation function. Correlated

overlap functions corresponding to quasi-hole states in closed-shell nuclei have been extracted from the asymptotic OBDM multipoles, $\rho_l(r, r')$, computed at large asymptotic distances $r' \leq 100$ fm. The reliability of the extraction method has been tested in the shell model, where a detailed study of the different fit procedures and of the convergence distances has been performed. These distances have been found to be very large in the cases in which two single-particle states of close energies are present. In those cases the asymptotic distances considered in our calculation of the OBDM have been enough to separate the corresponding overlap functions of the nuclei ^{12}C , ^{16}O and ^{40}Ca . As also has been found in other works [22, 33, 39], short-range correlations produce small effects on the density distribution and likewise on the OBDM. Our results given in figs. 7–9 show that these effects are more noticeable in the overlap functions since they are determined by the asymptotic behavior of the OBDM. Short-range correlations produce a redistribution of the single-particle densities in coordinate space. Their values are reduced at the maximum and increased for large distances. In the case of the valence shells we find a hardening of the distribution related to the collective effect of the NN repulsion at short distances.

The values of the computed spectroscopic factors in the present work are around 0.985, in accord with the findings obtained with other techniques. It is known that tensor and long-range correlations can reduce these values but, at present, no model is able to reproduce the experimental values extracted from $(e, e'p)$ data.

The computed overlap functions have been included in a DWIA model of the $(e, e'p)$ reaction, and exclusive response functions and cross sections have been computed for quasi-elastic kinematics. Although the computed spectroscopic factors are less than one, we have found an increase ($\sim 5\%$) of the response functions and, accordingly, of the cross section in the region of the maximum of the missing momentum distribution for knockout from the valence shells. This reduction is independent on the FSI and is a consequence of the increase of the single-particle densities for large distances. Thus the inclusion of central correlations is worsening the description of the experimental data in our model. This again proves that central correlations alone are not enough to describe this reaction successfully. Apart from spin-isospin and tensor correlations, not included here for computational reasons, we would like to remark the necessity of a model including in addition long-range correlations in a consistent way.

The later correlations are related to the presence of admixture of multi- $\hbar\omega$ configurations into the valence wave functions of the residual nucleus [40]. For instance in the case of the ^{40}Ca nucleus, the residual states correspond to the nucleus ^{39}K . It is known that the transverse form factors of the measured elastic and inelastic transitions in ^{39}K show significant departures from the single-particle picture and that a modification of the extreme shell model wave functions through the effect of core polarization is needed to describe the electron scattering cross section [40]. When computing the $(e, e'p)$ reaction in ^{40}Ca one uses a wave function which reproduces the elastic electron scattering data or equivalently, the charge density, corresponding to the initial state (the ground state of

^{40}Ca), ignoring the necessity of a proper description of the residual states also, usually treated as single holes in the core.

Concerning the (γ, p) reaction, central correlations play here a more important role, producing a large reduction of the cross section, since this reaction is sensitive to the high momentum components of the wave function where correlation effects are maximized.

In this paper we have demonstrated with a realistic model that the asymptotic method to compute the OBDM is feasible and that convergence of the results can be obtained: therefore it rises as an alternative, reliable starting point to be applied to other kind of correlated densities.

Acknowledgments

We would like to thank G. Co' for fruitful discussions. This work was supported by funds provided by DGICYT (Spain) under contracts PB/98-1367, PB/98-1318, and by the Junta de Andalucía (FQM225, FQM220).

A Multipole analysis of exclusive response functions

The general multipole analysis of the $(e, e'p)$ responses including polarization degrees of freedom of the target nucleus and electron was presented in refs. [23, 29]. The formalism can also be applied to the present case of $J = 0$ nuclei, where some simplification of the multipoles given in ref. [23] can be done. The following equations we write in this appendix have been obtained, after some work, from the corresponding equations of ref. [23] for the particular case $\mathcal{J} = 0$ (\mathcal{J} being in [23] the angular momentum corresponding to a multipole expansion in terms of spherical harmonics $Y_{\mathcal{J}\mathcal{M}}(\theta^*, \phi^*)$ of the nuclear polarization angles).

We expand the nuclear electromagnetic current as a sum of Coulomb (for the time component), and electric and magnetic (for the transverse three-vector current) multipole operators of rank J . The final hadronic state is also expanded in partial waves of the ejected proton, as a combination of hadronic states with total angular momentum J , denoted as $|\sigma\rangle \equiv |(lj)J_\alpha; J\rangle$, that represents a nucleon in the continuum with asymptotic angular momenta lj coupled with the residual nuclear state $|\Phi_\alpha^{(A-1)}\rangle = |J_\alpha\rangle$. The exclusive response functions can be written in the form

$$W^L = \frac{1}{K} \sum_{L \geq 0} [L] P_L^0(\cos \theta') W_L^L \quad (73)$$

$$W^T = \frac{1}{K} \sum_{L \geq 0} [L] P_L^0(\cos \theta') W_L^T \quad (74)$$

$$W^{TL} = -\frac{1}{K} \sum_{L \geq 1} \frac{[L]}{\sqrt{L(L+1)}} P_L^1(\cos \theta') W_L^{TL} \quad (75)$$

$$W^{TL'} = \frac{1}{K} \sum_{L \geq 1} \frac{[L]}{\sqrt{L(L+1)}} P_L^1(\cos \theta') W_L^{TL'} \quad (76)$$

$$W^{TT} = \frac{1}{K} \sum_{L \geq 2} \frac{[L]}{\sqrt{(L-1)L(L+1)(L+2)}} P_L^2(\cos \theta') W_L^{TT}, \quad (77)$$

with $[L] = \sqrt{2L+1}$. Note that the whole dependence on the emitted proton angle θ' is given through the Legendre functions $P_L^M(\cos \theta')$ and that the present response functions are divided by the factor $K = Mp'/(2\pi\hbar)^3$ respect to those of ref. [23]. The reduced response functions W_L^K , defined as the coefficients in the expansions (73–77) are given by

$$W_L^L = \sum_{\sigma'\sigma} \Phi_{\sigma'\sigma}(L) \begin{pmatrix} J & J' & L \\ 0 & 0 & 0 \end{pmatrix} \xi_{J'-l', J-l}^+ R_{\sigma'\sigma}^L \quad (78)$$

$$W_L^T = -\sum_{\sigma'\sigma} \Phi_{\sigma'\sigma}(L) \begin{pmatrix} J' & J & L \\ 1 & -1 & 0 \end{pmatrix} (\xi_{J'-l', J-l}^+ R_{\sigma'\sigma}^{T1} + \xi_{J'-l', J-l}^- R_{\sigma'\sigma}^{T2}) \quad (79)$$

$$W_L^{TL} = -2 \sum_{\sigma'\sigma} \Phi_{\sigma'\sigma}(L) \begin{pmatrix} J' & J & L \\ 0 & 1 & -1 \end{pmatrix} (\xi_{J'-l', J-l}^+ R_{\sigma'\sigma}^{TL1} - \xi_{J'-l', J-l}^- R_{\sigma'\sigma}^{TL2}) \quad (80)$$

$$W_L^{TL'} = -2 \sum_{\sigma'\sigma} \Phi_{\sigma'\sigma}(L) \begin{pmatrix} J' & J & L \\ 0 & 1 & -1 \end{pmatrix} (\xi_{J'-l', J-l}^+ I_{\sigma'\sigma}^{TL1} - \xi_{J'-l', J-l}^- I_{\sigma'\sigma}^{TL2}) \quad (81)$$

$$W_L^{TT} = -\sum_{\sigma'\sigma} \Phi_{\sigma'\sigma}(L) \begin{pmatrix} J' & J & L \\ 1 & 1 & -2 \end{pmatrix} (\xi_{J'-l', J-l}^+ R_{\sigma'\sigma}^{TT1} - \xi_{J'-l', J-l}^- R_{\sigma'\sigma}^{TT2}). \quad (82)$$

Note that the TL and TL' reduced response functions of ref. [23] include an extra factor $\sqrt{2}$ due to the different definition of the v_{TL} and $v_{TL'}$ factors. The coupling coefficient $\Phi_{\sigma'\sigma}(L)$ includes the internal sums over third components and it is defined as

$$\Phi_{\sigma'\sigma}(L) = P_{l+l'+L}^+ [J][J'][j][j'] [L] (-1)^{J+J'+J_\alpha+1/2+L} \begin{pmatrix} j' & j & L \\ \frac{1}{2} & -\frac{1}{2} & 0 \end{pmatrix} \left\{ \begin{matrix} j' & j & L \\ J & J' & J_\alpha \end{matrix} \right\} \quad (83)$$

We also use the parity functions

$$P_i^\pm = \frac{1}{2} [1 \pm (-1)^i] \quad (84)$$

$$\xi_{ij}^+ = (-1)^{(i-j)/2} P_{i+j}^+ \quad (85)$$

$$\xi_{ij}^- = (-1)^{(i-j+1)/2} P_{i+j}^-. \quad (86)$$

In order to define the functions $R_{\sigma',\sigma}^K$ and $I_{\sigma',\sigma}^K$ in eqs. (78)–(82), we introduce the Coulomb, electric and magnetic multipole matrix elements

$$C_\sigma \equiv \langle \sigma | \hat{M}_J(q) | 0 \rangle \quad (87)$$

$$E_\sigma \equiv \langle \sigma | \hat{T}_J^{el}(q) | 0 \rangle \quad (88)$$

$$M_\sigma \equiv \langle \sigma | i \hat{T}_J^{mag}(q) | 0 \rangle. \quad (89)$$

where $\hat{M}_J(q)$, $\hat{T}_J^{el}(q)$ and $\hat{T}_J^{mag}(q)$ are the usual Coulomb, electric and magnetic multipole operators. The functions $R_{\sigma',\sigma}^K$ and $I_{\sigma',\sigma}^K$ in eqs. (78)–(82) are then defined by the following quadratic forms constructed with these multipoles

$$R_{\sigma'\sigma}^L = \text{Re}[C_{\sigma'}^* C_{\sigma}] \quad (90)$$

$$R_{\sigma'\sigma}^{T1} = \text{Re}[E_{\sigma'}^* E_{\sigma} + M_{\sigma'}^* M_{\sigma}] \quad (91)$$

$$R_{\sigma'\sigma}^{T2} = \text{Re}[E_{\sigma'}^* M_{\sigma} - M_{\sigma'}^* E_{\sigma}] \quad (92)$$

$$R_{\sigma'\sigma}^{TL1} = \text{Re}[C_{\sigma'}^* E_{\sigma}] \quad (93)$$

$$R_{\sigma'\sigma}^{TL2} = \text{Re}[C_{\sigma'}^* M_{\sigma}] \quad (94)$$

$$I_{\sigma'\sigma}^{TL1} = \text{Im}[C_{\sigma'}^* E_{\sigma}] \quad (95)$$

$$I_{\sigma'\sigma}^{TL2} = \text{Im}[C_{\sigma'}^* M_{\sigma}] \quad (96)$$

$$R_{\sigma'\sigma}^{TT1} = \text{Re}[E_{\sigma'}^* E_{\sigma} - M_{\sigma'}^* M_{\sigma}] \quad (97)$$

$$R_{\sigma'\sigma}^{TT2} = \text{Re}[E_{\sigma'}^* M_{\sigma} + M_{\sigma'}^* E_{\sigma}]. \quad (98)$$

The L , T , TL and TT responses include only the real parts of the quadratic combinations of the various multipole matrix elements, while the fifth response function TL' is a linear combination of the imaginary parts (95,96). Therefore the TL' response is zero in PWIA, where the matrix elements (87–89) are real numbers. In presence of an interaction, however, the matrix elements (87–89) are in general complex numbers, due to the asymptotic complex phase $e^{i\delta_{lj}}$ introduced by the nuclear interaction in the wave function, and as a consequence, the fifth response function is different from zero in DWIA. The sum over the quantum numbers $\sigma = (l, j, J)$, $\sigma' = (l', j', J')$ and L in eqs. (73)–(82) is only restricted by angular momentum conservation. In practical calculations we fix the number of multipoles involved in the sums by comparing our results with the ones corresponding to the factorized PWIA in the impulse approximation where, as known, the nuclear responses can be computed exactly.

The outgoing proton wave function corresponds to a solution of the Schrödinger equation for positive energies using a complex optical potential fitted to elastic proton-nucleus scattering data. The partial wave lj with energy $E > 0$ and wave number $k = \sqrt{2ME}$ is determined by the asymptotic condition

$$R_{lj}(k, r) \sim \sqrt{\frac{2M}{\pi\hbar^2 k}} e^{-i(\sigma_l + \delta_{lj}^*)} \sin\left(kr - \eta \log 2kr - l\frac{\pi}{2} + \sigma_l + \delta_{lj}^*\right) \quad (99)$$

where δ_{lj} is the complex phase-shift and σ_l is the Coulomb phase-shift. In the limit in which the imaginary part of the optical potential is zero, the phase-shift δ_{lj} a real number, the continuum radial wave functions are normalized with a Dirac delta function containing the energies (see Ref. [23]). The imaginary (absorptive) part of the optical potential modifies the normalization of the continuum states since the flux of the outgoing particles in the elastic channel is reduced.

B Asymptotic OBDM for unoccupied states

We consider as an example the simplest case of the multipole $l = 2$ for the nucleus ^{12}C . More details are given in [34]. We use the expression (43) for the correlated contributions to the OBDM. First we exclude the contribution of diagrams C and D of fig. 2, since the dependence of these terms on the density coordinates \mathbf{r}, \mathbf{r}' is done across the non correlated density $\rho_0(\mathbf{r}, \mathbf{r}')$ which only contains the multipoles $l = 0, 1$ in the case of ^{12}C . In other words, the external points \mathbf{r} and \mathbf{r}' in diagrams C and D are connected with the others with density lines only, which cannot modify its multi-polarity $l = 0, 1$.

In the case of diagram A of fig. 2, it can be written in a multipole expansion as [22]

$$\begin{aligned} \rho_A(\mathbf{r}_1, \mathbf{r}'_1) &= \sum_{n_1 l_1 j_1} (2j_1 + 1) R_{n_1 l_1 j_1}(r_1) R_{n_1 l_1 j_1}(r'_1) \sum_{l_2} \frac{2l_2 + 1}{2l_2 + 1} \begin{pmatrix} l_1 & l_2 & l \\ 0 & 0 & 0 \end{pmatrix}^2 P_l(\cos \theta_{11'}) \\ &\times \int_0^\infty dr_2 r_2^2 \rho_0(r_2) f_{l_2}(r_1, r_2) f_{l_2}(r'_1, r_2) \end{aligned} \quad (100)$$

where the function $f_{l_2}(r_1, r_2)$ is the multipole of the correlation function for angular momentum l_2 . The sum over n_1, l_1, j_1 corresponds to the occupied states $1s_{1/2}$ e $1p_{3/2}$ in ^{12}C . The multipole $l = 2$ of the OBDM is obtained as the coefficient of the Legendre polynomial $P_2(\cos \theta_{11'})$ in the above equation. Since we are interested in the asymptotic behavior for $r_1, r'_1 \rightarrow \infty$ we only consider the contribution coming from the $l_1 = 1$ term, i.e., $(n_1 l_1 j_1) = 1p_{3/2}$. Hence the 3- j coefficient gives a non zero result for $l_2 = 1$ only. The corresponding multipole $l_2 = 1$ for the correlation function is proportional to the integral

$$\int d \cos \theta_{12} \cos \theta_{12} f(\mathbf{r}_{12}) = -A \int d \cos \theta_{12} \cos \theta_{12} e^{-B r_{12}^2} \sim -\frac{A}{2B r_1 r_2} e^{-B(r_1 - r_2)^2}. \quad (101)$$

Hence the asymptotic behavior of the $l = 2$ multipole for $r_1, r'_1 \rightarrow \infty$ is

$$\rho_A(r_1, r'_1)_{l=2} \sim R_{1p_{3/2}}(r_1) R_{1p_{3/2}}(r'_1) \int_0^\infty dr_2 r_2^2 \rho_0(r_2) \frac{e^{-B(r_1 - r_2)^2}}{r_1 r_2} \frac{e^{-B(r'_1 - r_2)^2}}{r'_1 r_2}. \quad (102)$$

Changing to the variable $r'_2 = r_2 - r_m$, where $r_m = (r_1 + r'_1)/2$ is the mid point between r_1 and r'_1 , we arrive to

$$\rho_A(r_1, r'_1)_{l=2} \sim R_{1p_{3/2}}(r_1) R_{1p_{3/2}}(r'_1) \frac{e^{-B(r_1 - r'_1)^2/2}}{r_1 r'_1} \rho_0(r_m) \int_{-\infty}^\infty dr'_2 e^{-2B r'^2_2}. \quad (103)$$

Finally, introducing the asymptotic behavior of the radial functions

$$R_{1p_{3/2}}(r_1) \sim \frac{e^{-kr_1}}{r_1} \quad (104)$$

$$\rho(r_m) \sim \frac{e^{-2kr_m}}{r_m^2} = 4 \frac{e^{-k(r_1 + r'_1)}}{(r_1 + r'_1)^2}, \quad (105)$$

we obtain the following asymptotic expression

$$\rho_A(r_1, r'_1)_{l=2} \sim \frac{\exp(-2kr_1) \exp(-2kr'_1) \exp\left(\frac{-B(r_1-r'_1)^2}{2}\right)}{r_1^2 r_1'^2 (r_1 + r'_1)^2} \quad r_1, r'_1 \rightarrow \infty. \quad (106)$$

A similar expression can be obtained for diagram B of fig. 2.

References

- [1] J. J. Kelly, *Adv. Nucl. Phys.* **23** (1996) 75.
- [2] S. Boffi, C. Giusti, F. D. Pacati, M. Radici, *Electromagnetic response of atomic nuclei*, Oxford University Press (1996).
- [3] G. Van der Steenhoven, P. K. A. de Witt Huberts, in *Modern Topics in Electron Scattering*, B. Frois and I. Sick eds., World Scientific (1991) 510.
- [4] L. Lapikás, *Nucl. Phys.* **A553** (1993) 297c.
- [5] P. K. A. de Witt Huberts, *J. Phys. G: Nucl. Part. Phys* **16** (1990) 507.
- [6] M. Leuschner *et al.*, *Phys. Rev.* **C49** (1994) 955.
- [7] J.M. Udías, P. Sarriguren, E. Moya de Guerra, E. Garrido and J.A. Caballero, *Phys. Rev.* **C48** (1993) 2731; *Phys. Rev.* **C51** (1995) 3246.
- [8] M. Radici, S. Boffi, S. C. Pieper, V. R. Pandharipande, *Phys. Rev.* **C50** (1994) 3010.
- [9] D. Van. Neck, M. Waroquier, A. E. L. Dieperink, S. C. Pieper and V. R. Pandharipande, *Phys. Rev.* **C57** (1998) 2308.
- [10] A. Polls, M. Radici, S. Boffi, W. H. Dickhoff and H. Müther, *Phys. Rev.* **C55** (1997) 810.
- [11] A. Polls, H. Müther and W. H. Dickhoff, *Phys. Rev.* **C51** (1995) 3040.
- [12] H. Müther, A. Polls and W. H. Dickhoff, *Nucl. Phys.* **A594** (1995) 117.
- [13] H. Müther, A. Polls, *Prog. Part. and Nucl. Phys.* 45 (2000) 243.
- [14] W. J. W. Geurts, K. Allaart, W. H. Dickhoff and H. Müther, *Phys. Rev.* **C 53** (1996) 2207.
- [15] D. V. Neck, L. Van Daele, Y. Dewulf and M. Waroquier *Phys. Rev.* **C 56** (1997) 1398.
- [16] A. E. L. Dieperink and T. de Forest, Jr., *Phys. Rev.* **C 10** (1974) 543.

- [17] D. V. Neck, M. Waroquier and K. Heyde, Phys. Lett. **B314** (1993) 255.
- [18] D. V. Neck, A. E. L. Dieperink and M. Waroquier, Phys. Rev. **C 53** (1996) 2231.
- [19] M. V. Stoitsov, S. S. Dimitrova, A. N. Antonov, Phys. Rev. **C53** (1996) 1254.
- [20] S. S. Dimitrova, M. K. Gaidarov, A. N. Antonov, M. V. Stoitsov, P. E. Hodgson, V. K. Lukyanov, E. V. Zemlyanaya and G. Z. Krumova, J. Phys. G: Nucl. Part. Phys. **23** (1997) 1685.
- [21] M. K. Gaidarov, K. A. Pavlova, A. N. Antonov, M. V. Stoitsov, S. S. Dimitrova and C. Giusti, Phys. Rev. **C61** (2000) 014306.
- [22] F. Arias de Saavedra, G. Co' and M. M. Renis, Phys. Rev. **C55** (1997) 673.
- [23] J.E. Amaro and T.W. Donnelly, Ann. Phys. (N.Y.) **263** (1998) 56.
- [24] J. E. Amaro and T. W. Donnelly, Nucl. Phys. **A646** (1999) 187.
- [25] J.E. Amaro, J. A. Caballero, T. W. Donnelly, A. M. Lallena, E. Moya de Guerra and J. M. Udias, Nucl. Phys. **A602** (1996) 263.
- [26] J. M. Udias, J. A. Caballero, E. Moya de Guerra, J. E. Amaro and T. W. Donnelly, Phys. Rev. Lett. **83** (1999) 5451.
- [27] J. Gao *et al.*, Phys. Rev. Lett. **84** (2000) 3265.
- [28] T. Berggren, Nucl. Phys. **72** (1965) 337.
- [29] A.S. Raskin and T.W. Donnelly, Ann. Phys. (NY) **191** (1989), 78.
- [30] J. E. Amaro, A. M. Lallena, J. A. Caballero, Phys. Rev. **C60** (1999) 014602.
- [31] J.E. Amaro, J.A. Caballero, T.W. Donnelly and E. Moya de Guerra, Nucl. Phys. **A611** (1996) 163.
- [32] F. Arias de Saavedra, G. Co', A. Fabrocini and S. Fantoni, Nucl. Phys. **A605** (1996) 359.
- [33] A. Fabrocini and G. Co', Phys. Rev. **C63** (2001) 044319.
- [34] M. Mazziotta, Thesis, University of Pisa, 2001, unpublished.
- [35] P. Schwandt *et al.*, Phys. Rev **C26** (1982) 55.
- [36] L. Chinitz *et al.*, Phys. Rev. Lett. **67** (1991) 568.
- [37] G.J. Miller *et al.*, Nucl. Phys. **A586** (1995) 125.
- [38] J.I. Johansson, H.S. Sherif and F. Ghoddoussi, Nucl. Phys. **A 665** (2000) 403.

- [39] A. Fabrocini, F. Arias de Saavedra and G. Co', Phys. Rev. **C 61** (2000) 044302.
- [40] P.G. Blunden, Phys. Lett. **B164** (1985) 258; P.G. Blunden and B. Castel, Nucl. Phys. **A445** (1985) 742.